8-6-2009

Experimental Design, Data Analysis, and Modeling for Characterizing the Three-Dimensional Acoustic Field of a Seismic Airgun Array

Arslan Tashmukhambetov
University of New Orleans

Experimental Design, Data Analysis, and Modeling for Characterizing the Three-Dimensional Acoustic Field of a Seismic Airgun Array

A Dissertation

Submitted to the Graduate Faculty of the
University of New Orleans
in partial fulfillment of the
requirements for the degree of

Doctor of Philosophy
in
Engineering and Applied Science

by

Arslan M. Tashmukhambetov

B.S. Physics Kazakh State University, 2003
M.S. Physics University of Louisiana at Lafayette, 2005

August 2009

Acknowledgements

I would like to acknowledge my friends, colleagues, professors, faculty members, and staff from Department at the Physics of University of New Orleans for their kind support, help, and encouragement during all my education years in the PhD program. Without their participation it was almost impossible for me to get the appropriate stimulus to conduct this dissertation research, achieve good results, publish an article in the Journal of the Acoustical Society of America, and be deeply involved as a scientist in underwater acoustics and related areas.

I would like to personally acknowledge Drs. George and Juliette Ioup of UNO and Dr. Natalia Sidorovskaia of the Physics Department of University of Louisiana at Lafayette who literally replaced my parents all the years I was studying abroad and were personally involved in my everyday activities.

I would like to acknowledge the Industry Research Funding Coalition and the Joint Industry Programme (JIP) who financially supported my research through the International Association of Oil and Gas Producers (OGP) and the International Association of Geophysical Contractors (IAGS).

I would like to acknowledge the members of the Project Study Group (PSG) of JIP for their excellent supervising, valuable consulting, and intensive participation in the research project I was working on all these years.

I would like to acknowledge my dissertation committee members, Dr. Abu K. Mostofa Sarwar of the Earth Sciences Department, Dr. Dimitrios Charalampidis of the Department of Electrical Engineering, Drs. George and Juliette Ioup of the Department of Physics, and Dr. Natalia Sidorovskaia for their guidance, understanding, patience, flexibility and time generosity in the course of this research.

Table of Contents

List of Figures

Abstract

In June 2003, the Littoral Acoustic Demonstration Center conducted an acoustic characterization experiment for a standard seismic exploration array. Two moorings with Environmental Acoustic Recording Systems (EARS) were deployed in the northern part of the Gulf of Mexico to measure ambient noise and collect shot information. A 21-element seismic airgun array was towed along five parallel linear tracks with horizontal closest approach points to the EARS buoy position of 63, 500, 1000, 2000, and 5000 m. Calibrated acoustic pressure measurements collected during the experiment were analyzed to obtain zero-to-peak sound pressures, sound exposure levels, and pressure levels in 1/3-octave frequency bands. In addition, the experimental data were modeled by using a modified underwater acoustic propagation model to fill in missing data measurements. The resulting modeling procedure showed good agreement between measured and modeled data in absolute pressure amplitudes and frequency interference patterns for frequencies up to 1000 Hz. The analysis is important for investigating the potential impact on marine mammals and fish and predicting the exposure levels for newly planned seismic surveys in other geographic areas.

Based on results of the experiment conducted and data analysis performed, a new experimental design was proposed to maximize the amount of collected data using the available equipment while minimizing the time needed for the source ship. The design used three patches, one with 3º angular spacing between the lines at a reference depth. Embedded is a smaller patch with 1º spacing and within that a still smaller patch with one half degree spacing. This arrangement gives a reasonably uniform distribution of shots versus solid angle with a large variety of emission and azimuthal angles for different ranges. Due to the uncertainty of positioning systems, the angular space is divided into solid angle bins. Simulations predicted more than 200 shots per bin for emission angles greater than 13 degrees. Statistical analysis of collected data will be performed on the proposed bin basis. An experiment based on the proposed design was conducted in Fall 2007. The data measurements collected during the experiment are currently being analyzed and will be reported in the near future.

Keywords: Airgun array characterization, airgun array, seismic airgun array, underwater acoustics, acoustical data analysis, hydrophone measurements, acoustic propagation modeling.

Chapter 1 Overview

The main tool used by oil companies to explore for hydrocarbons beneath the ocean is a seismic airgun array towed behind a source ship. The airgun array consists of individual guns which release compressed air to generate acoustic pulses. They are towed near the surface and the combination of the direct pulse and the surface reflected pulse constitute the primary source signal from the airgun. Although many experiments have been done to measure the properties of seismic airgun arrays, some of them proprietary, there has not been a major experiment to completely characterize the three-dimensional primary acoustic field of the array. In 2003 the source ship, MV Kondor, was in the Gulf of Mexico to do a controlled exposure experiment with sperm whales. Three different groups had hydrophones in the water to make limited measurements of the acoustic field. One group, the Littoral Acoustic Demonstration Center (LADC), had a moored hydrophone pair at a depth of 750 m. The pair consisted of a sensitive phone to measure ambient noise and a desensitized phone which could measure the airgun array in close proximity without clipping. At the end of the controlled exposure experiment, the Kondor ran five tracks for recording by LADC. One was directly over the moored hydrophone and the others had horizontal offsets of 500 m, 1000 m, 2000 m, and 5000 m. The analysis of this experiment has been published in the Journal of the Acoustical Society of America (Tashmukhambetov et al., 2008), and it forms Chapter 3 of this dissertation. As a result of that careful experiment using calibrated hydrophones, LADC was approached by the oil industry to conduct a detailed study of the hydrophone three-dimensional field. The 2003 experiment was funded by the Industry Research Funding Coalition through the International Association of Geophysical Contractors (IAGC). The detailed study is funded by a consortium of oil industry partners through the International Association of Oil and Gas Producers (OGP). This effort is part of multiple environmental projects funded by the consortium under the name Joint Industry Programme (JIP). Each project is overseen by a Project Study Group (PSG). In particular, there is a PSG for the seismic airgun characterization experiment, headed by Dr. Michael Jenkerson of ExxonMobil, which has worked closely with the LADC consortium partners. One of the first tasks for LADC was to design the experiment which would make the measurements needed to completely characterize the three-dimensional field of the seismic airgun array. The resulting design is discussed in Chapter 4.

LADC is a consortium of scientists from UNO (the University of New Orleans), USM (the University of Southern Mississippi), ULL (the University of Louisiana at Lafayette), NRL (the Naval Research Laboratory) at Stennis Space Center, NAVOCEANO (the Naval Oceanographic Office) and the Applied Research Laboratories of the University of Texas at Austin. All institution but the last participated in these experiments.

This dissertation gives an overview of the mathematical description of acoustic propagation in a fluid in Chapter 2. It gives the derivation of the linear wave equation for a fluid medium. This linear wave equation is both space and time dependent. It can be reduced to the Helmholtz differential equation by applying the separation of variables technique. The Helmholtz equation is a second order differential equation which is a function of space variables only. It can be further simplified by taking into account azimuthal symmetry, the paraxial approximation, and factorization, which lead to a first order parabolic equation. Solution to the parabolic equation can be found by further approximating the equation operators, in this case by the Pade approximation (Collins, 1993).

The 2003 experiment is described in Chapter 3, which is adapted from an article published in the Journal of Acoustical Society of America (Tashmukhambetov *et. al.,* 2008). The first part after an introduction gives detailed information about the experimental broadband measurements of absolute pressures output from the seismic exploration array. The second part of the chapter has a description and results of the modeling procedure adapted and used to model measured absolute pressure during the described experiment.

The experimental design developed by LADC, which was led by the dissertation author, is described in Chapter 4. It was developed for characterizing the three-dimensional primary acoustic field of a seismic airgun array and specifies both the tracks of a dedicated source vessel and hydrophone placement in the water column. The experiment has been done and the data collected. Intensive analysis of the data is now underway. The data are also being modeled. Future publications will report on these phases.

Results of the designed experiment and future research guidelines are summarized in the last part of this dissertation.

Chapter 2 Underwater acoustic wave propagation

2.1 Wave Equation

The propagation of acoustic waves in the ocean obeys the nonlinear acoustic wave equation. In the case of small flows and small perturbations quadratic terms responsible for the nonlinear effects can be neglected and the nonlinear wave equation can be linearized. The resulting linear acoustic wave equation can be developed from a set of three linear equations – the continuity equation, the force equation (Euler's equation), and the equation of state (Kinsler *et al.*, 1982).

The equation of state describes the thermodynamical behavior of the substance and relates such thermodynamical properties as pressure P, density ρ and temperature T. For ideal gases the equation of state has the following form

$$PV = nRT \; or \; P = r\rho T, \tag{2.1.1}$$

where r = specific gas constant, R = gas constant, and n = number of moles.

By their nature acoustical processes are nearly isentropic, i.e., adiabatic and reversible, so acoustic behavior of an ideal gas is directed by the adiabat

$$\frac{P}{P_0} = \left(\frac{\rho}{\rho_0}\right)^{\gamma}, \tag{2.1.2}$$

where γ is the ratio of specific heats, P_0 is the ambient pressure, and ρ_0 is the ambient density.

For fluids other than an ideal gas, the adiabat is more complicated and the equation of state can be represented by a Taylor's series expansion

$$P = P_0 + \left(\frac{\partial P}{\partial \rho}\right)_{\rho_0} (\rho - \rho_0) + \frac{1}{2}\left(\frac{\partial^2 P}{\partial \rho^2}\right)_{\rho_0} (\rho - \rho_0)^2 + \cdots \tag{2.1.3}$$

For small acoustic fluctuations only the lowest order terms need to be kept, which gives a linear relationship between pressure fluctuation and change in the medium density

$$p = P - P_0 = \left(\frac{\partial P}{\partial \rho}\right)_{\rho_0} (\rho - \rho_0) = B\frac{\rho - \rho_0}{\rho_0} = Bs, \tag{2.1.4}$$

where p = acoustic pressure, $B = \rho_0 \left(\frac{\partial P}{\partial \rho}\right)_{\rho_0}$ = adiabatic bulk modulus, and $s = \frac{\rho - \rho_0}{\rho_0}$ = condensation (change in density).

The equation of continuity describes the relationship between fluid particle velocity $\vec{u}$ and instantaneous density ρ

$$\frac{\partial \rho}{\partial t} + \nabla \cdot (\rho \vec{u}) = 0. \tag{2.1.5}$$

Because ambient density ρ_0 does not change with time or position and condensation s is usually a very small number, the continuity equation becomes

$$\frac{\partial \rho}{\partial t} + \nabla \cdot (\rho \vec{u}) = \frac{\partial}{\partial t}(1+s)\rho_0 + \nabla \cdot \left((1+s)\rho_0 \vec{u}\right) = \frac{\partial s}{\partial t} + \nabla \cdot \vec{u} = 0. \tag{2.1.6}$$

The general form of Euler's force equation is given by

$$\rho \frac{d\vec{u}}{dt} + \nabla P = 0. \tag{2.1.7}$$

This equation can be reduced to linear form for acoustic waves of small amplitude by substituting expressions for density ρ and pressure P and neglecting small order terms to produce

$$\rho \frac{d\vec{u}}{dt} + \nabla P = (\rho_0 - \rho_0 s)\left(\frac{\partial}{\partial t}\vec{u} + (\vec{u} \cdot \nabla)\vec{u}\right) + \nabla(P_0 + p) = \rho_0 \frac{\partial \vec{u}}{\partial t} + \nabla p = 0. \tag{2.1.8}$$

Taking the time derivative of the linear continuity equation (2.1.6) and the divergence of the linear Euler's equation (2.1.8), rearranging terms, and substituting one in the other results in the linear acoustic wave equation

$$\frac{\partial}{\partial t}\left(\frac{\partial s}{\partial t} + (\nabla \cdot \vec{u})\right) = \frac{\partial^2 s}{\partial t^2} + \nabla \cdot \left(\frac{\partial \vec{u}}{\partial t}\right) = \frac{1}{B}\frac{\partial^2 p}{\partial t^2} + \nabla \cdot \left(\frac{\partial \vec{u}}{\partial t}\right) = 0\,,$$

$$\nabla \cdot \left(\rho_0 \frac{\partial \vec{u}}{\partial t} + \nabla p\right) = \rho_0 \nabla \cdot \left(\frac{\partial \vec{u}}{\partial t}\right) + \nabla^2 p = 0,$$

$$\nabla^2 p - \frac{\rho_0}{B}\frac{\partial^2 p}{\partial t^2} = \nabla^2 p - \frac{1}{c^2}\frac{\partial^2 p}{\partial t^2} = 0, \tag{2.1.9}$$

where $c = \sqrt{\frac{B}{\rho_0}}$ is the thermodynamic speed of sound.

Equation (2.1.9) is the linear lossless wave equation for propagation of sound in fluids with phase speed c. Since during the derivation we never used any restrictions on the adiabatic bulk modulus or ambient pressure with respect to the space, this equation is valid for acoustic wave propagation in media with sound speeds that are functions of space, such as the ocean.

2.2 Helmholtz Equation

The linear acoustic wave equation (2.1.9) can be reduced to the homogeneous Helmholtz differential equation by using the separation of variables technique (Kinsler *et al.*,1982)

$$\mathrm{p}(\vec{\mathrm{r}}, \mathrm{t}) = \mathrm{A}(\vec{\mathrm{r}})\mathrm{T}(\mathrm{t}) \rightarrow \nabla^2 p - \frac{1}{c^2}\frac{\partial^2 p}{\partial t^2} = \mathrm{T}\nabla^2\mathrm{A} - \mathrm{A}\frac{1}{c^2}\frac{d^2\mathrm{T}}{dt^2} = 0,$$

$$\mathrm{T}\nabla^2\mathrm{A} = \mathrm{A}\frac{1}{c^2}\frac{d^2\mathrm{T}}{dt^2} \rightarrow \frac{\nabla^2\mathrm{A}}{\mathrm{A}} = \frac{1}{Tc^2}\frac{d^2\mathrm{T}}{dt^2},$$

$$\frac{\nabla^2\mathrm{A}}{\mathrm{A}} = -k^2 \rightarrow \nabla^2\mathrm{A} + k^2A = (\nabla^2 + k^2)A = 0, \tag{2.2.1}$$

$$\frac{1}{Tc^2}\frac{d^2\mathrm{T}}{dt^2} = -k^2 \rightarrow \frac{d^2\mathrm{T}}{dt^2} + k^2c^2T = \left(\frac{d^2}{dt^2} + \omega^2\right)T = 0, \tag{2.2.2}$$

where ω = angular frequency, and k is the magnitude of the wave vector $\vec{k}$, the vector wavenumber.

The solution of the time dependant equation (2.2.2) will be a linear combination of sine and cosine functions, with angular frequency ω, while the form of the solution for the homogeneous Helmholtz equation (2.2.1) in space will depend on boundary conditions.

Because of the presence of the source of acoustic waves in a medium we have to solve the inhomogeneous Helmholtz equation

$$(\nabla^2 + k^2)A(\vec{\mathrm{r}}) = LA(\vec{\mathrm{r}}) = f(\vec{\mathrm{r}}), \tag{2.2.3}$$

where $f(\vec{\mathrm{r}})$ is a source function which describes the source of the waves, and $L = \nabla^2 + k^2$ is the Helmholtz operator.

This equation (2.2.3) can be solved by using a Green's function. Green's function $G(\vec{\mathrm{r}}, \vec{\mathrm{r}}_0)$ is a function which satisfies the following equation (Bayin, 2006)

$$LG(\vec{\mathrm{r}}, \vec{\mathrm{r}}_0) = \delta(\vec{\mathrm{r}} - \vec{\mathrm{r}}_0). \tag{2.2.4}$$

If such a function $G(\vec{\mathrm{r}}, \vec{\mathrm{r}}_0)$ can be found for the operator L, then if we multiply equation (2.2.4) by the source function, and then integrate over the $\vec{\mathrm{r}}_0$ variable we will obtain

$$\int LG(\vec{\mathrm{r}}, \vec{\mathrm{r}}_0)\ f(\vec{\mathrm{r}}_0)\mathrm{d}\vec{\mathrm{r}}_0 = \int \delta(\vec{\mathrm{r}} - \vec{\mathrm{r}}_0)f(\vec{\mathrm{r}}_0)\mathrm{d}\vec{\mathrm{r}}_0 = f(\vec{\mathrm{r}}) = LA(\vec{\mathrm{r}}).$$

Since the operator $L = L(\vec{\mathrm{r}})$ is linear and independent of the integration variable $\vec{\mathrm{r}}_0$, we can take it outside the integral and find the general expression for the solution of equation (2.2.3)

$$L\int G(\vec{\mathrm{r}}, \vec{\mathrm{r}}_0)\ f(\vec{\mathrm{r}}_0)\mathrm{d}\vec{\mathrm{r}}_0 = LA(\vec{\mathrm{r}}),$$

$$A(\vec{\mathrm{r}}) = \int G(\vec{\mathrm{r}}, \vec{\mathrm{r}}_0)\ f(\vec{\mathrm{r}}_0)\mathrm{d}\vec{\mathrm{r}}_0. \tag{2.2.5}$$

2.3 Parabolic Equation

Complete analytic solutions describing wave propagation in an oceanic medium can be found for cases with no or linear variation in the sound speed with the depth, and range independence. All other situations require using numerical approach in the solution. A variety of different numerical methods was

developed during the previous several decades. The parabolic equation (Levy, 2000) approach based on a numeric Pade's rational approximation was used for this thesis research.

We will substitute the Laplace operator expression in cylindrical coordinates into the homogeneous Helmholtz equation (2.2.1)

$$\nabla^2 = \frac{1}{r}\frac{\partial}{\partial r}\left(r\frac{\partial}{\partial r}\right) + \frac{1}{r^2}\frac{\partial^2}{\partial \theta^2} + \frac{\partial^2}{\partial z^2}, \tag{2.3.1}$$

$$(\nabla^2 + k^2)A(\vec{r}) = \left(\frac{1}{r}\frac{\partial}{\partial r}\left(r\frac{\partial}{\partial r}\right) + \frac{1}{r^2}\frac{\partial^2}{\partial \theta^2} + \frac{\partial^2}{\partial z^2} + k^2\right)A(r,\theta,z) = 0. \tag{2.3.2}$$

Because the oceanic environment is assumed to be azimuthally independent, the second term of the Laplace operator is equal to zero

$$\frac{1}{r^2}\frac{\partial^2}{\partial \theta^2}A(r,\theta,z) = 0 \rightarrow A = A(r,z),$$

$$\left(\frac{1}{r}\frac{\partial}{\partial r}\left(r\frac{\partial}{\partial r}\right) + \frac{\partial^2}{\partial z^2} + k^2\right)A(r,z) = 0. \tag{2.3.3}$$

$A(r,z)$ is written as $A(r,z) = \frac{1}{\sqrt{r}}u(r,z)$ and expanded

$$\left(\frac{1}{r}\frac{\partial}{\partial r}\left(r\frac{\partial}{\partial r}\right) + \frac{\partial^2}{\partial z^2} + k^2\right)\frac{1}{\sqrt{r}}u(r,z) =$$

$$= \frac{1}{\sqrt{r}}\frac{\partial^2}{\partial z^2}u(r,z) + \frac{1}{\sqrt{r}}\frac{\partial^2}{\partial r^2}u(r,z) + \frac{1}{4r^2}\frac{1}{\sqrt{r}}u(r,z) + k^2\frac{1}{\sqrt{r}}u(r,z) = 0. \tag{2.3.4}$$

The paraxial approximation states that $\frac{1}{4r^2}\frac{1}{\sqrt{r}}u(r,z)$ is negligibly small for distant ranges resulting in

$$\frac{\partial^2}{\partial z^2}u(r,z) + \frac{\partial^2}{\partial r^2}u(r,z) + k^2u(r,z) = 0. \tag{2.3.5}$$

We can define two operators $P_{operator} = \frac{\partial}{\partial r}$, and $O_{operator} = \sqrt{\frac{1}{k^2}\frac{\partial^2}{\partial z^2} + \frac{\omega^2}{c^2k^2}}$, and rewrite (2.3.5) in the following way

$$\left(P^2{}_{operator} + k^2O^2{}_{operator}\right)u(r,z) = 0. \tag{2.3.6}$$

Equation (2.3.6) can be factored into two equations governing backward and forward acoustic wave propagation

$$\left(P_{operator} + ik \cdot O_{operator}\right)\left(P_{operator} - ik \cdot O_{operator}\right)u(r,z) = 0. \tag{2.3.7}$$

Since we have no interest in the backscattered field, only the equation responsible for forward propagation will be considered. Expressions for the operators are substituted in (2.3.7)

$$P_{operator}u(r,z) = ik \cdot O_{operator}u(r,z),$$

$$\frac{\partial}{\partial r}u(r,z) = ik \cdot \sqrt{\frac{1}{k^2}\frac{\partial^2}{\partial z^2} + \frac{\omega^2}{c^2k^2}} \cdot u(r,z) = i \cdot \frac{\omega}{c}\sqrt{1 + \frac{c^2}{\omega^2}\frac{\partial^2}{\partial z^2}} \cdot u(r,z). \quad (2.3.8)$$

We will perform a change of variables $u(r,z) = p(r,z)e^{-ik_o r}$ and replace terms $\frac{\omega}{c} = k_o, \frac{c^2}{\omega^2}\frac{\partial^2}{\partial z^2} =$ X, resulting in

$$\frac{\partial}{\partial r}p(r,z) = i \cdot k_o\left(-1 + \sqrt{1 + X}\right) \cdot p(r,z). \quad (2.3.9)$$

Numerical solution to the first order differential equation (2.3.9) is given by Collins (1993)

$$p(r + \Delta r, z) = \exp\left[ik_o \Delta r\left(-1 + \sqrt{1 + X}\right)\right] \cdot p(r,z), \quad (2.3.10)$$

where the expression in the exponential can be approximated by Pade's polynomial expansion

$$\exp\left[ik_o \Delta r\left(-1 + \sqrt{1 + X}\right)\right] = 1 + \sum_{j=1}^{n} \frac{a_{j,n}X}{1 + b_{j,n}X}. \quad (2.3.11)$$

The final numerical solution for equation (2.3.2) is given by

$$A(r,z) = \frac{e^{-ik_0 r}}{\sqrt{r}}p(r,z), p(r + \Delta r, z) = \left(1 + \sum_{j=1}^{n} \frac{a_{j,n}X}{1 + b_{j,n}X}\right) \cdot p(r,z). \quad (2.3.12)$$

This numerical solution is implemented in the Range-Dependant Acoustic Model (RAM) developed by Michael Collins (1993).

Chapter 3 Three-dimensional seismic array characterization study: Experiment and modeling

3.1 Introduction

In the last decade a considerable amount of effort has been focused on understanding how sound generated by human-made acoustic sources in the ocean may influence marine mammals. One of the important aspects of this effort is the measurement and prediction of the broadband acoustic energy distribution of such sources in complex, variable ocean waveguides. Seismic exploration arrays are of interest for environmental impact assessment (Gordon *et al*., 2004). These arrays comprise a collection of airguns distributed over an array geometry and towed behind a seismic vessel. They are designed to fire synchronously and produce powerful highly-directional bottom-directed pulses to image acoustically the sub-bottom structure. The geophysical response is primarily analyzed in the low frequency band up to 300 Hz (Caldwell and Dragoset, 2000). Hence, the higher frequency component of acoustic radiation from has been mostly overlooked until concerns were raised about the effect of this radiation on marine species, especially marine mammals, that rely on acoustics as a survival tool (for orientation, food foraging, communication, etc.). Recent studies of individual sperm whale communication codas strongly suggest that frequencies above 1000 Hz are of particular importance in sperm whale communication (Ioup *et al.*, 2005). This frequency range may overlap with the high frequency component of seismic array radiation. On-whale tag recordings during controlled exposure experiments conducted in the Northern Gulf of Mexico (GoM) in 2002 and 2003 showed that received peak pressures and sound exposure levels (SEL's) of tagged whales do not necessarily decrease as the range between the whale and the seismic array increases under certain circumstances, such as constructive interference of overlapping arrivals, the presence of a surface duct, etc. (Madsen *et al.*, 2006). Reported data show that absolute received pressure levels can be as high at 12 km as they are at 2 km. It strongly suggests that spherical and cylindrical spreading approaches should not be automatically used to determine impact zones and that animal SEL should be determined from existing waveguide propagation conditions and three-dimensional source array directional patterns.

There are discussions in the underwater acoustic community and oil industry about the results of quantitative studies of the effects of waveguide propagation including surface ducts, which are formed seasonally in the GoM, on acoustic energy distribution (MacGillivray, 2006; DeRuiter *et al.*, 2006; Tolstoy *et al.*, 2004). Surface ducts can form a series of energetically powerful precursor pulses (arriving before the main energy associated with the direct arrival) spread throughout the entire depth of the water column with a range decay rate slower than that of the direct arrival (Labianca, 1972; Monjo and DeFerrari, 1994; Sidorovskaia and Werby, 1995; Sidorovskaia, 2004). Therefore, an animal at any depth

can be exposed to significant levels of acoustic energy that are not associated with the direct arrival. Hence, waveguide propagation modeling should become an indispensable part of the development of any mitigation metrics. Both calibrated measurements and quantitative modeling of a seismic array energy distribution for a full range of angles and emitted frequencies become the first steps in our ability to predict and mitigate any potentially negative effects.

Experimental calibrated measurements of the broadband absolute pressure output from an industrial seismic exploration airgun array, which has been collected by the Littoral Acoustic Demonstration Center (LADC) in June 2003 for three-dimensional seismic source characterization studies, will be presented in the second and third paragraphs of this chapter. LADC, which was founded in 2001, currently is a consortium of scientists from three universities (the University of New Orleans, the University of Southern Mississippi, and the University of Louisiana at Lafayette) and the Naval Research Laboratory at Stennis Space Center. Since 2001, LADC has conducted or participated in eight experiments in the Northern GoM and the Mediterranean Sea to study natural and anthropogenic noise in marine environments and the potential impact on marine mammals (Newcomb *et al.*, 2002a, 2002b; Newcomb *et al.*, 2005; Sidorovskaia *et al.*, 2006; Tashmukhambetov *et al.*, 2006). The results of quantitative modeling of measured absolute pressures by using enhanced modeling techniques based on standard underwater acoustic propagation model [the range dependent acoustic model (RAM)] will be presented in the fourth paragraph of this chapter .

3.2 Experiment

3.2.1 Source/receiver configuration

LADC deployed Environmental Acoustic Recording System (EARS) buoys developed by the Naval Oceanographic Office. Two single channel EARS buoys (25 kHz bandwidth) were collocated on the same mooring near Green's Canyon in the Northern GoM (27° 40.0995' N, 90° 21.9660'W) during June 2003 for a seismic characterization experiment. One buoy hydrophone recorded ambient noise and the other was desensitized (by 12.7 dBV) to record marine seismic array emissions without clipping the data.

The hydrophone of each buoy was approximately 250 m from the bottom in a water depth of about 990 m. Only the data from the desensitized EARS hydrophone are discussed in this chapter. The M/V Kondor towed a 21-element seismic airgun array of total volume of 3590 in.^{3} (0.0588 m.^{3}) on five parallel linear tracks with horizontal closest approach points to the EARS buoy position of 63, 500, 1000,

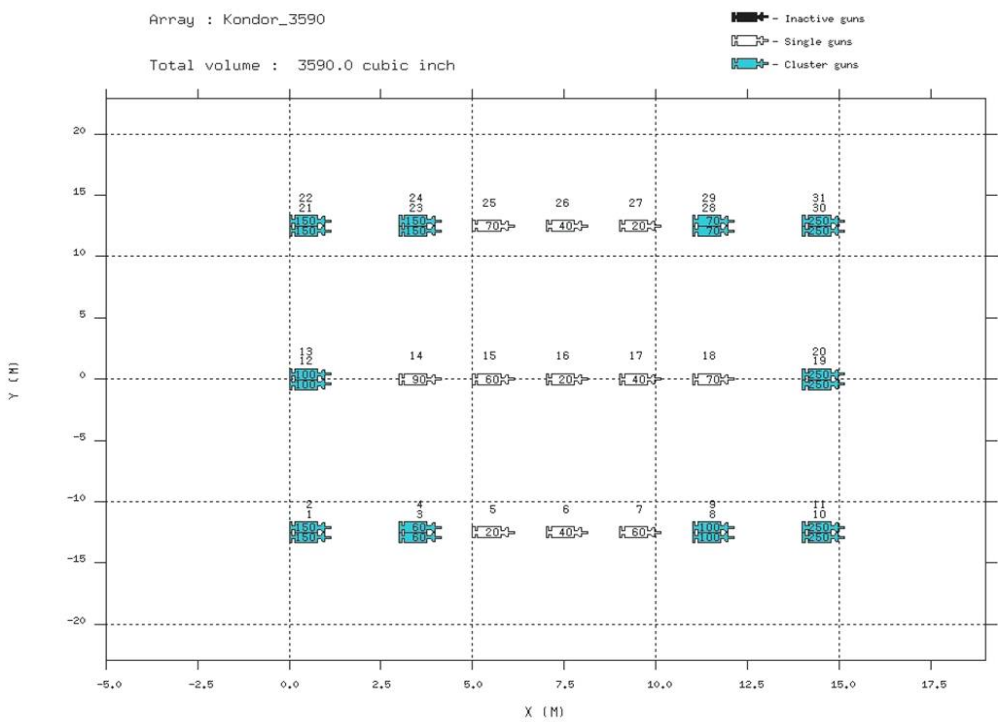

Figure 3.2.1 The M/V Kondor seismic array configuration for the seismic characterization experiment. The numbers inside each airgun indicate the individual volume in in.^{3} of each airgun.

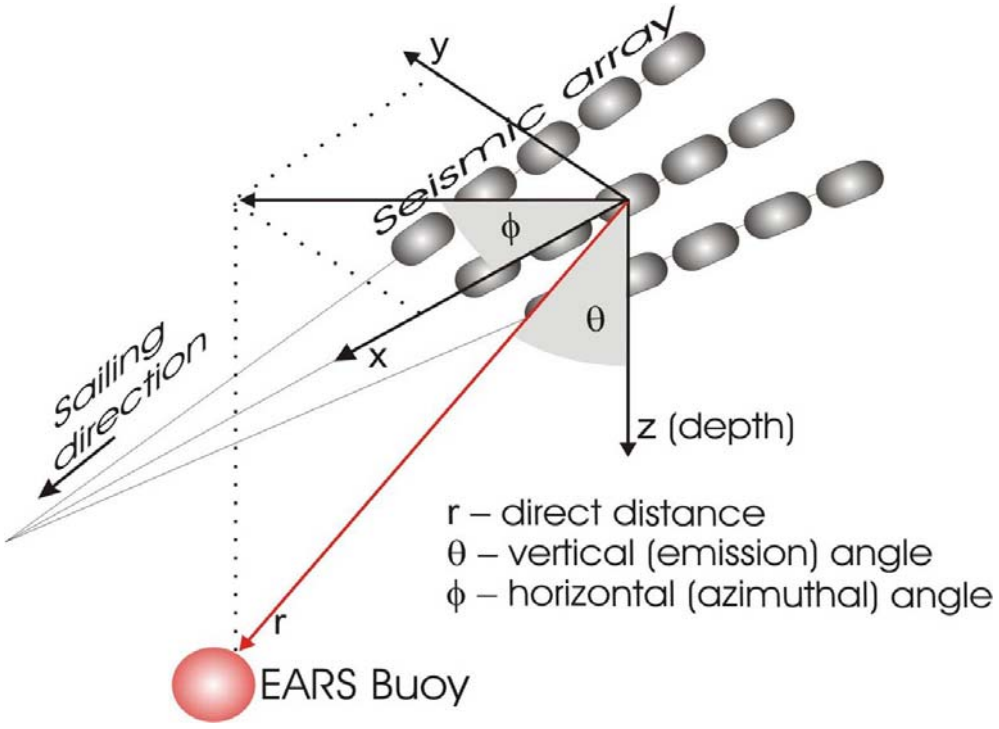

Figure 3.2.2 Reference coordinate system with the origin at the array center.

2000, and 5000 m. The seismic array configuration is shown in Figure 3.2.1. Figure 3.2.2 shows the reference coordinate system used in this research to characterize the array directionality. The emission angle θ is the angle between the vertical and a line connecting the position of the array center and a receiving hydrophone. The azimuthal angle ϕ is measured in the horizontal plane with 0° directly in front of the array, 180° directly behind, 90° to starboard, and 270° to port. The tracks provide a wide range of measured emission angles (6°–84°, with 0° corresponding to the vertical) and horizontal ranges up to 7 km from the array center to the EARS buoys. The Kondor tracks (labeled as line 0.2, line 500, line 1000, line 2000, and line 5000) are illustrated in Figure 3.2.3. The total number of shots recorded was about 500.

3.2.2 Experimental data calibration

In order to obtain absolute measured sound pressure levels, it is important that the recording equipment calibrations be fully understood. Figure 3.2.4 is a block diagram of the data acquisition flow in a typical EARS buoy. Two calibration methods have been implemented for the EARS buoys. The first method, which is often called a frequency-domain method since the result is a direct function of frequency, involves injecting a single narrowband sine wave into the electronics downstream of the hydrophone. The input voltage magnitude and phase of the injected signal are compared to the output voltage. This is repeated for many different frequencies to obtain the transfer function of the equipment across a broad frequency band. In the other method, which is often called the time-domain method since the result is a direct function of time, a temporally very short signal (4.7 μs long) is injected into the electronics downstream of the hydrophone. The temporally short characteristic of this "impulse" results in a very wide band of frequencies. The output is recorded and is a direct measure of the impulse response of the equipment. Ideally, the impulse response of the equipment and the transfer function of the equipment are Fourier transform pairs and will lead to the same final results when appropriately applied to the raw data. For the LADC 2003 experiment, a comparison of the two methods for the desensitized EARS buoy yielded the same results between 6 Hz and 25 kHz. Since the time-domain method requires the use of more complicated deconvolution techniques to remove the impulse response from the recorded data, all final calibrations of the recorded data were performed using the frequency-domain method. It must be noted that neither of the above methods of calibration includes the response of the hydrophone itself. This must be included in the final calibration of the acoustic data to obtain absolute pressure levels. The hydrophone transfer functions have been determined by the manufacturer. Figure 3.2.5 illustrates 200 ms of acoustic data corresponding to the direct arrivals from an array emission near the closest point of

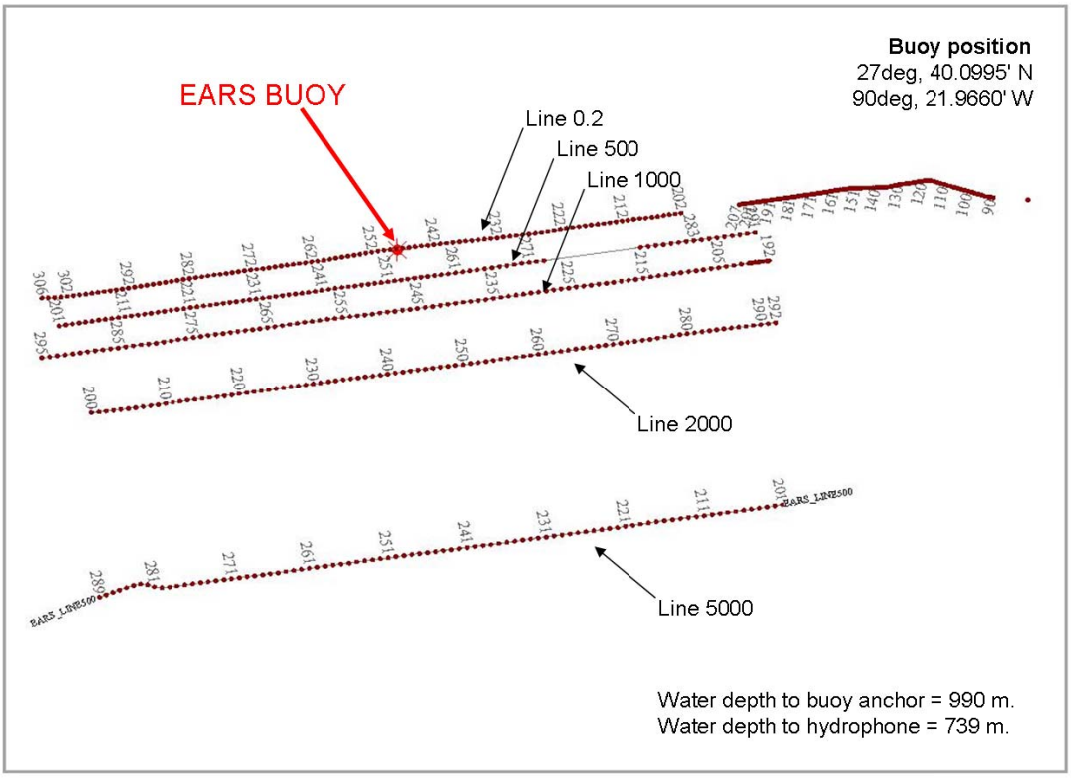

Figure 3.2.3 The M/V Kondor line/shot diagram in the horizontal plane. The nominal seismic array depth is 6.7 m below the surface.

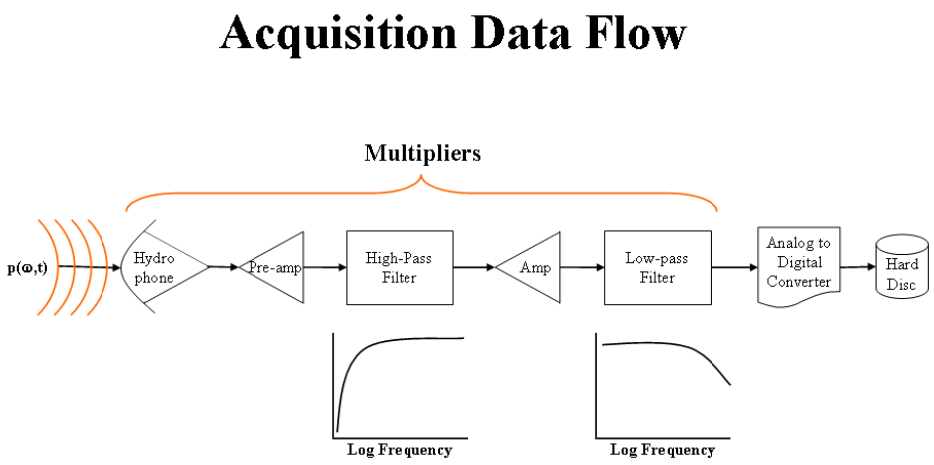

Figure 3.2.4 Block diagram illustrating the data flow in a typical acoustic data acquisition system and the components that affect final data calibration.

approach (CPA) of the array to the EARS buoy. The upper plot is the raw data in volts and the bottom plot is the same data segment in micropascals after all the calibrations have been applied. The EARS response (including the hydrophone) is nearly flat from 6 Hz to 25 kHz so that the two plots have very little difference except in units. We will restrict our analyses of the data to this calibrated frequency band (6 Hz to 25 kHz).

3.3 Experimental data analysis: methods and results.

Seismic arrays are designed to be highly directional in order to focus the low-frequency sound energy in the vertical direction for the purpose of seismic exploration. The probability that a marine mammal will be exposed to the near vertical downward propagating direct pulse is fairly small. This is not so with off-axis acoustic emissions, so studies of off-axis acoustic signatures are of special interest. Hence, multipath propagation and leakage of high-frequency energy from the airgun array into the ocean waveguide are critical issues for studying the impact on marine mammals. Figures 3.3.1–3 show a series of absolute acoustic pressures versus time recorded during the experiment and the corresponding spectrograms for individual shots on different tracks with different horizontal ranges from the center of the array to the buoy location and different emission and azimuthal angles. The spectrograms $S(f_k, t_m)$ are calculated over a 5 ms window with 20% overlap,

$$
\begin{gathered}
S(f_k, t_m) = 20 \cdot \log\{|\sqrt{2}F(k,m)|\}, \qquad k = 1, \ldots, \frac{N}{2} - 1, \\
F(k,m) = \Delta t \sum_{j=1}^{N-1} p[(j + N_s m)\Delta t]\, e^{-\frac{i2\pi jk}{N}}, \\
k = 0,1, \ldots, N-1, m = 0, \ldots, M
\end{gathered}
\tag{3.3.1}
$$

where $F(k,m)$ are complex Fourier coefficients obtained from a standard fast Fourier transform program; $p(j\Delta t)$ are calibrated temporal pressure samples; N=390 is the number of pressure samples in a 5 ms analysis window; Δt=1.28×10^{-5} s is the sampling interval for the collected data; $f_k = \Delta f \cdot k, \Delta f = \frac{1}{\Delta t \cdot N}, k = 0,1, \ldots, \frac{N}{2}$; $N_s = N \cdot 0.8$ is the temporal index shift in terms of pressure sample number for 20% overlap; $M = N_0/N_s$ is the integer number of spectral windows in a 2 s spectrogram. The calculation of the Fourier coefficients in equation (3.3.1) reflects the transient nature of the measured seismic signatures that should be considered finite energy signals, not power signals. (Fricke *et al.*, 1985; Johnston *et al*., 1988). Instead of the power flux spectral density traditionally analyzed for infinitely long stationary signals, an energy flux spectral density $\varepsilon(k)$ is quantified in the calibration procedure for marine seismic source transient signals (Fricke *et al.*, 1985):

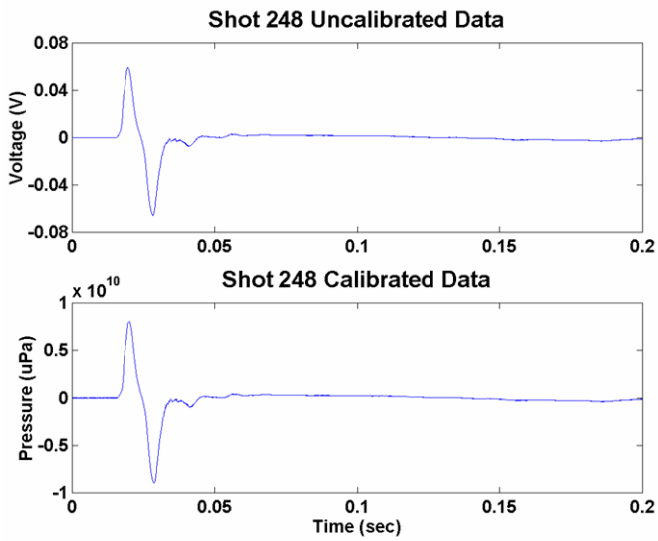

Figure 3.2.5 Calibration results for 200 ms of acoustic data corresponding to the direct arrivals from an airgun shot near the CPA of the array to the EARS buoy. The upper plot shows the raw data in V and the bottom plot shows the same data segment in μPa after all the calibrations have been applied. The EARS response (including the hydrophone) is nearly flat from 6 Hz to 25 kHz so that the two plots have very small differences except in units.

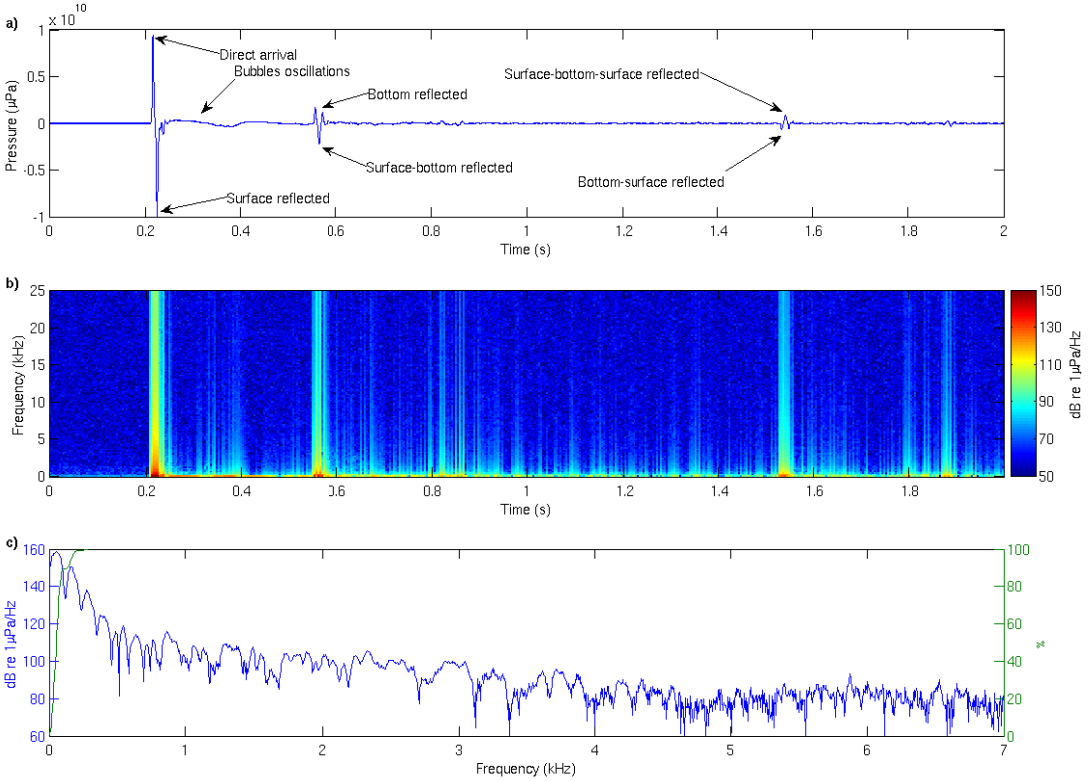

Figure 3.3.1 (a) Measured absolute calibrated acoustic pressure for the CPA shot 249 on line 0.2 vs. time. The horizontal range is 63 m, the direct distance to the hydrophone is 736 m, the emission angle is 5°, and the azimuthal angle is 202°. (b) Spectrogram of the signal in (a) using a 5 ms rectangular window with 20% overlap from 6 Hz to 25 kHz. (c) The calibrated amplitude spectrum over a 2 s rectangular window with a start time corresponding to the 0.2 s temporal mark of the spectrogram in (b) and cumulative energy flux in % vs. frequency.

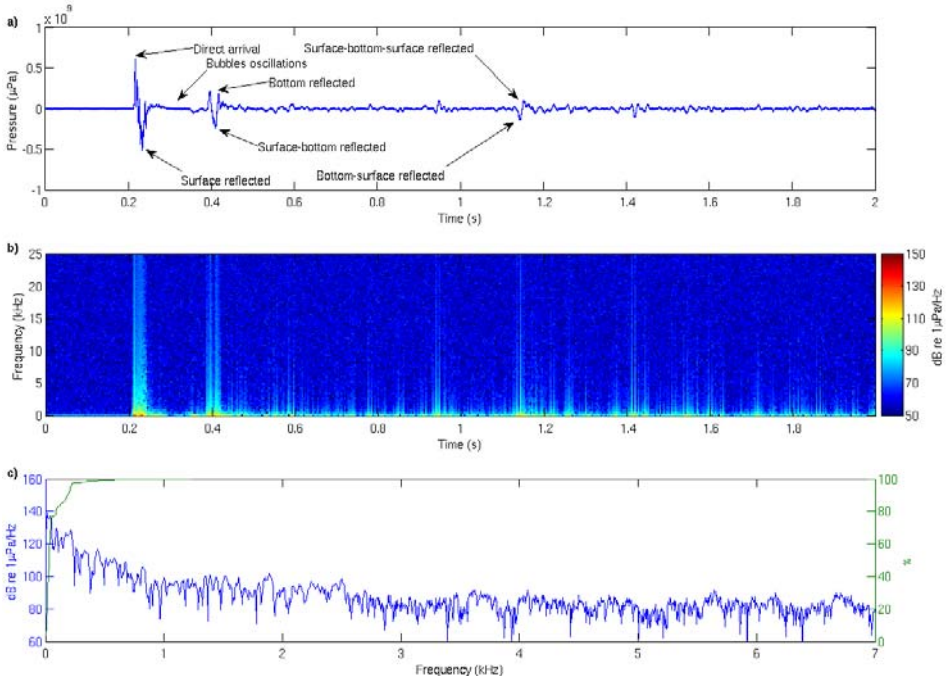

Figure 3.3.2(a) Measured absolute calibrated acoustic pressure for shot 235 on line 1000 vs. time. The horizontal range is 1655 m, the direct distance to the hydrophone is 1810 m, the emission angle is 66°, and the azimuthal angle is 144°. (b) Spectrogram of the signal in (a) over a 5 ms rectangular window with 20% overlaps from 6 Hz to 25 kHz. (c) The calibrated amplitude spectrum over a 2 s rectangular window with a start time corresponding to the 0.2 s temporal mark of the spectrogram in (b) and cumulative energy flux in % vs. frequency.

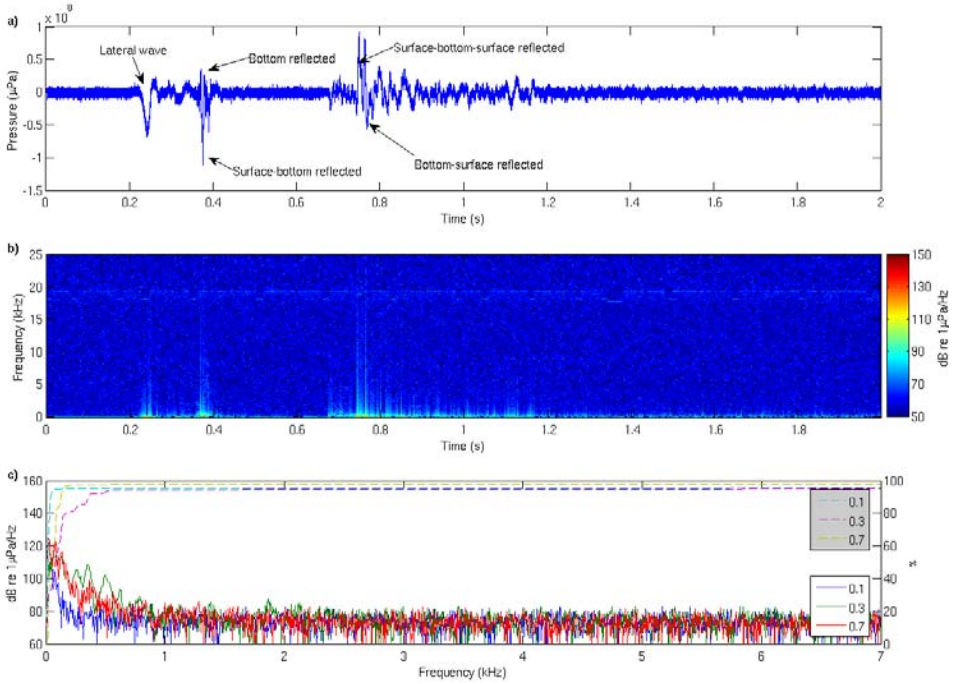

Figure 3.3.3 (a) Measured absolute calibrated acoustic pressure for shot 211 on line 5000 vs. time. The horizontal range is 6197 m, the direct distance to the hydrophone is 6240 m, the emission angle is 83°, and the azimuthal angle is 128°. (b) Spectrogram of the signal in (a) over a 5 ms rectangular window with 20% overlaps from 6 Hz to 25 kHz. The lateral (head) wave precursor is the first arrival. High frequencies are attenuated as would be expected for a lateral wave. (c) The calibrated amplitude spectra over a 0.2 s rectangular window with start times corresponding to the 0.15, 0.35, and 0.65 s temporal marks of the spectrogram in (b) and cumulative energy fluxes (%) vs. frequency.

$$\varepsilon(k) = \frac{1}{\rho c}|F(k)|^2, \tag{3.3.2}$$

where $F(k)$ is the discrete Fourier transform coefficient, which is defined in equation (3.3.1) for a single m value, ρ is the water density at the receiver position, and c is the speed of sound at the measuring point. The energy flux spectral density curve has the same shape as the amplitude spectrum (absolute values of the Fourier coefficients) but different units (J/(m^{2}Hz)). For a decibel scale, the amplitude spectrum level (referenced to 1 μPa) is 182 dB larger than the energy flux spectral density level (referenced to 1 (J/(m^{2}Hz)) if the acoustic impedance of sea water is approximated by the constant value

$$Z = \rho c = 1026\frac{kg}{m^3} \times 1500\frac{m}{s} \cong 1.54 \times 10^6\ Pa\frac{s}{m}.$$

Following SEG standards for specifying marine seismic energy sources (Johnston *et al.*, 1988), cumulative energy flux $u(k)$ and total energy flux $u(N/2)$ are calculated for the experimental data,

$$\begin{aligned} u(k) &= \Delta f \varepsilon(0) + 2\Delta f \sum_{l=1}^{k} \varepsilon(l), \qquad k = 1, \dots, \frac{N}{2} - 1, \\ u(0) &= \Delta f \varepsilon(0), \qquad u\left(\frac{N}{2}\right) = u\left(\frac{N}{2} - 1\right) + \Delta f \varepsilon\left(\frac{N}{2}\right). \end{aligned} \tag{3.3.3}$$

The cumulative energy flux corresponds to the amount of energy flux in a frequency band from 0 Hz to $k\Delta f$. The total energy flux is the cumulative energy flux in the full recorded frequency band. The cumulative energy flux is usually expressed as a percentage of the total energy flux,

$$\tilde{u}(k) = \frac{u(k)}{u\left(\frac{N}{2}\right)} \times 100\%, \qquad k = 0,1, \dots, N/2. \tag{3.3.4}$$

Figure 3.3.1(a) shows the measured calibrated pressure in micropascals for the closest approach point on line 0.2, which corresponds to a horizontal range of 63 m, with a direct distance to the hydrophone of 736 m, emission angle of 5°, and azimuthal angle of 202°. The 2 s shot spectrogram is shown in Figure 3.3.1(b). The amplitude spectrum level and cumulative energy flux for the 200 ms Fourier analysis window with a start time corresponding to the 0.2 s mark on the spectrogram plot are in Figure 3.3.1(c). The direct arrival, surface reflected arrival, bottom reflected arrival, bubble oscillation cycle, and multiples can be clearly identified in Figures 3.3.1(a) and 3.3.1(b). The separation between the direct and bottom reflected arrivals is 340 ms. The maximum amplitude spectrum power level is 159 dB re 1 μPa/Hz, with the level reaching 110 dB re 1 μPa/Hz at 1000 Hz for the direct arrival and 85 dB re 1 μPa/Hz at 5000 Hz for the direct arrival. The calculated total energy flux is 0.32 J/m^2. The sound propagation geometry to the EARS buoy for this shot is nearly vertical for the direct and bottom reflected pulses. The seismic arrays are tuned for optimal (near vertical) transmission of low frequencies for this geometry. The cumulative energy flux plot in Figure 3.3.1(c) shows that most of the energy is under

300 Hz. This is consistent with the array design. The high frequencies are about 35 dB lower than the 300 Hz level. Semiquantitative comparison from Figure 3.3.1(b) shows that the direct path signal energy flux spectral density level is about 20 dB greater at most high frequencies than the bottom reflected arrival and the multiples.

Figures 3.3.2(a)-3.3.2(c) show similar plots for shot 235 on line 1000. The horizontal range is 1655 m, the direct distance to the hydrophone is 1810 m, the emission angle is 66°, and the azimuthal angle is 144°. The calculated total energy flux is 0.0017 J/m^2. The arrival structure is still identifiable and labeled in Figures 3.3.2(a) and 3.3.2(b). The separation between the direct and bottom reflected arrivals is decreased to 200 ms. This may potentially indicate an increased sound exposure level vs. range to the shot for an animal having a 200 ms energy integration window (as discussed below). The maximum amplitude spectrum power level is 125 dB re 1 μPa/Hz, with the level reaching 100 dB re 1 μPa/Hz at 1000 Hz for the direct arrival and 80 dB re 1 μPa/Hz at 5000 Hz for the direct arrival, which is close to the background noise level. Figure 3.3.2(c) shows again that most of the energy is at a low frequency, under 500 Hz. At this range, the difference is about 25 dB between the high frequency and the 500 Hz levels. Figures 3.3.3(a)-3.3.3(c) present the data for shot 211 on line 5000. The horizontal range is 6197 m, the direct distance to the hydrophone is 6240 m, the emission angle is 83°, and the azimuthal angle is 128°. The signal is more complicated and the interpretation of the arrival pattern is not as straightforward as for the shots shown in Figures 3.3.1 and 3.3.2. The spectra reveal that most of the energy of the precursor is below 300 Hz. As one can see from the moveout of the signal with different shots on line 5000 in Figure 3.3.4, the temporal separation between the precursor and the main energy arrival increases with range. An additional analysis of the signal moveout curves for other lines indicates that the precursor starts appearing at ranges larger than 4.5 km. These features of the precursor arrival strongly suggest that it is a lateral (head, interface) wave. Correlation of experimental time delays between arrivals with modeled ones is required to gain more confidence concerning the analysis of the precursor. The frequency partition of energy for the various components of this shot is similar to that shown in the previous two figures. The amplitude spectrum level and cumulative energy flux for the 200 ms Fourier analysis window for three identifiable arrivals with start times corresponding to 0.15, 0.35, and 0.65 s on the spectrogram plot are shown in Figure 3.3.3(c). The calculated total energy fluxes are 0.028×10^{-3}, 0.023×10^{-3}, and 0.051×10^{-3} J/m^2. The high-frequency level reaches 90 dB re 1 μPa/Hz at 1000 Hz for the strongest arrival and this is close to the background noise level.

Figures 3.3.1-3.3.4 clearly demonstrates that there is a significant multipath energy in the sound field of the seismic array. The conclusion is that the acoustic energy in the multipath must be taken into account when calculating marine mammal exposure metrics, as suggested by Madsen *et al*. (2006). This

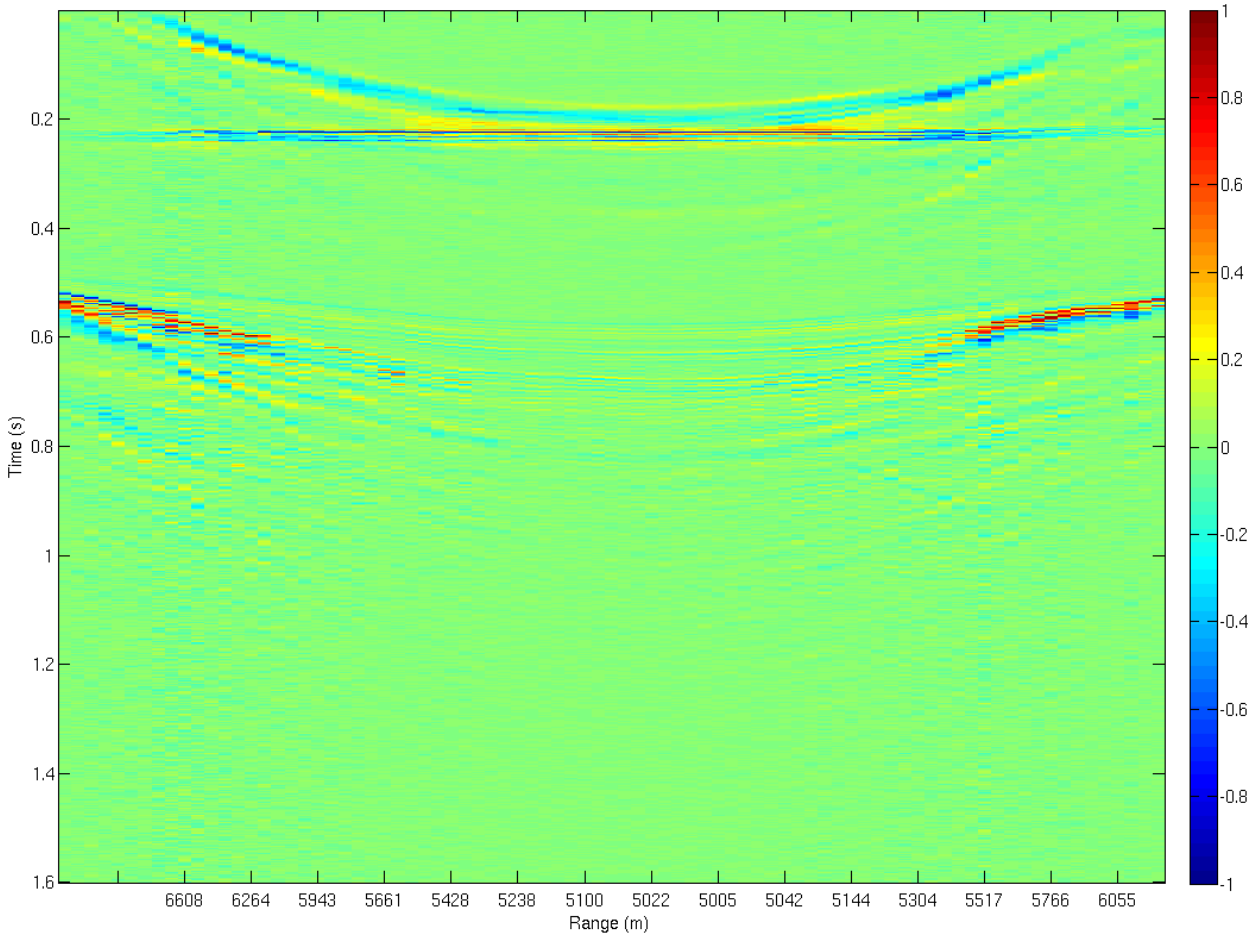

Figure 3.3.4 Normalized signal moveout map for line 5000 shots. The time is synchronized on the first bottom reflection. Each shot pressure function is normalized by the absolute value of the maximum pressure in this shot. The separation between a precursor and a reference strongest arrival increases with range.

can only be done accurately by using propagation models to calculate the full sound field for the waveguide environment.

Sequential 2 s amplitude spectra for all calibrated shots are collected in Figure 3.3.5. The high-frequency part of the spectrum (16–21 kHz) is shown separately in Figure 3.3.5(b), which allows better identification of the narrow spectral lines centered at 18 kHz. These represent the spectral content of the on-board echo-sounder signal. A Simrad EA500 echo-sounder was part of the M/V Kondor equipment suite and emitted a 3 ms pulse every 12 s throughout the duration of the experiment. It is apparent from Figure 3.3.5 that the high frequency acoustic power levels from the seismic array as recorded by the EARS buoy at 739 m depth do not approach the levels of the echo sounder, at least for ranges below 7 km.

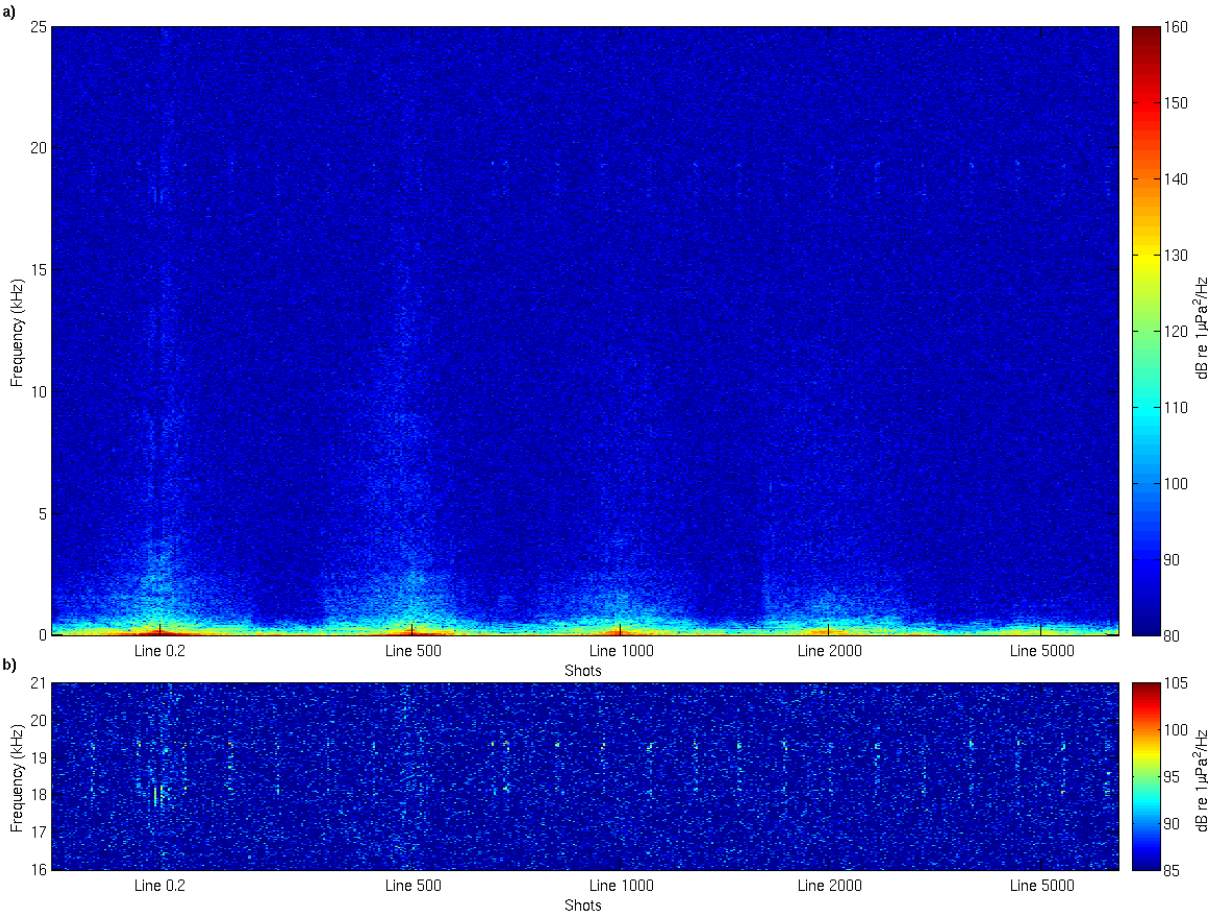

Figure 3.3.5(a) Sequential spectra of all calibrated shots collected over a 2 s rectangular window during the seismic characterization experiment from 6 Hz to 25 kHz. (b) High-frequency band (16–21 kHz) of the sequential spectra presented in (a). The short vertical lines centered at 18 kHz are spectra of the 3 ms pulses from an 18 kHz echo sounder on the M/V Kondor. It had a repetition rate of 12 s.

Various analysis attributes are generated to quantify and characterize the acoustic output of the seismic airgun array in the ocean in addition to the time and frequency analyses already given. The results shown here can easily be compared to the other studies presented in the literature (Blackwell *et al.*, 2004; Madsen *et al.*, 2006). The first characteristic widely accepted in the oil industry is the maximum received pressure level, zero to peak. (Some authors report a peak-to-peak value for far-field signatures, which will not be more than 3 dB greater than the zero-to-peak level.) Figure 3.3.6(a) shows the maximum received pressure level for each shot collected during the experiment. The maximum level for the closest shot almost directly overhead (horizontal range of 63 m, direct distance to the hydrophone of 736 m, and emission angle of 5°) is 200 dB re 1 μPa. Figure 3.3.6(b) shows the same data as a function of the horizontal range to the EARS buoy. The multivalued levels at a fixed range are due to array directionality and gun volume differences on the front versus the back of the array [see Figure 3.2.1(a)]. The maximum received pressure levels do not gradually decrease with increasing range beyond 3 km for off-axis shots.

They can be as high at the 5 km range as at the 3 km range due to waveguide propagation effects. These results are consistent with data recorded on sperm whales using acoustic tags during controlled exposure experiments (Madsen *et al.*, 2006). Solid and dashed curves represent the modeled maximum levels as a function of range in the vertical 0° plane aligned with the central line of the array obtained by using the parabolic equation model, RAM (Collins, 1993), and two notional source signature models: GUNDALF and NUCLEUS (Hatton, 2004; Nucleus) The details of the modeling are described in the next section. The modeled data do not reproduce all the features of measured data because the array directionality in different vertical planes is not taken into account due to computational time limitations. Next step in modeling procedures is moving to parallel cluster computers to implement full three-dimensional field modeling. Maximum levels of direct and reflected arrivals are important measures of the seismic array signal directionality and attenuation in a waveguide and provide meaningful information for seismic interpretation characterizing the reflection strength of different sub-bottom reflectors, but they cannot be used as standalone parameters to account for acoustic sensation by a marine mammal because they do not take the duration of the transient seismic pulses into account. It is suggested that most biological receivers, including marine mammals, are best modeled as energy integrators, which integrate intensity over a frequency-dependent time window (Au *et al.*, 1997; Madsen, 2005). The integration time of 200 ms is chosen because it is believed to be used as an integration time by the auditory system of the endangered sperm whale. Therefore, a second attribute, SEL, is calculated over the time of each shot as

$$\begin{aligned} SEL(i,t_j) &= 10\log\left\{\Delta t \sum_{m=0}^{N-1} p_i^2(t_j + m\Delta t)\right\} \\ &= 10\log\left\{\Delta f \sum_{k=0}^{N-1} |F_i(k,t_j|^2\right\} = 10\log\left\{Zu_i(\frac{N}{2},t_j)\right\}, \end{aligned} \tag{3.3.5}$$

where i is the shot number in the line, Δt=1.28×10^{-5} s is the temporal sampling interval of the recorded data, N =15 625 corresponds to a 200 ms integration window, p_i is the sampled recorded calibrated pressure (in micropascals) for shot i, and t_j is the initial time for a 200 ms analysis window for every possible start time within each shot including 200 ms of ambient noise recording before the first seismic arrival for each shot. The maximum SEL calculated for each shot is selected to characterize that shot. The maximum SEL for each shot in every line (sequentially) is displayed in Figure 3.3.7(a). The maximum value for the above-mentioned closest shot is 177 dB re 1 μPa^2 s. In Figure 3.3.7(b), the maximum SEL is shown as a function of the horizontal range between the center of the array and the receiving hydrophone. Solid and dashed lines are modeled sound exposure levels in the vertical 0° plane passing through the central line of the array. There are several factors that cause the maximum SEL to increase with range at ranges larger than 3 km. The first factor is that the temporal separation between the

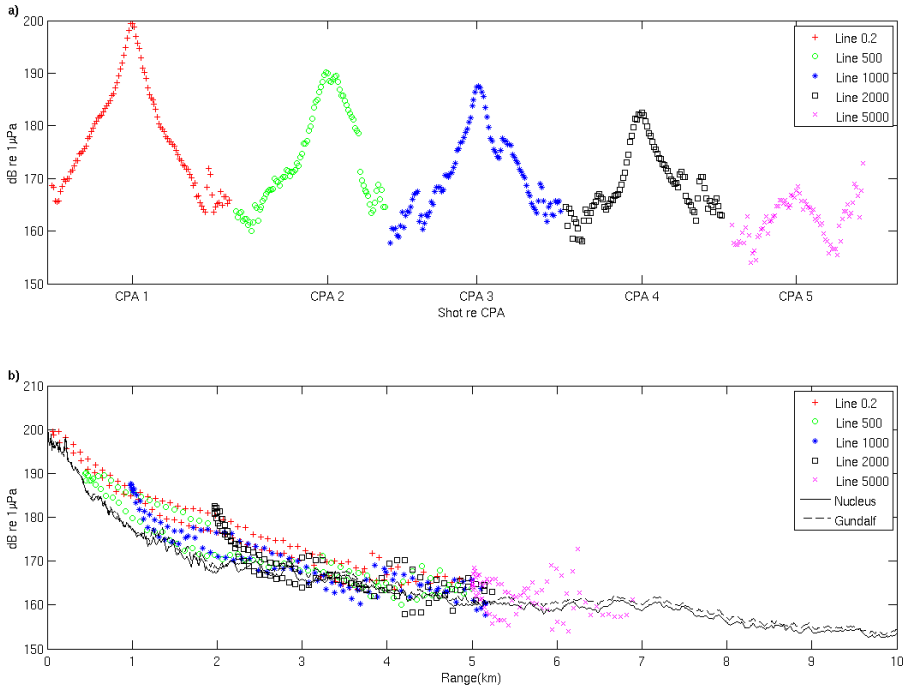

Figure 3.3.6 (a) Maximum received calibrated zero-to-peak sound pressure levels for each shot relative to the CPA indicated by the CPA marker on the horizontal axis for each line. (b) Maximum received zero-to-peak sound pressure levels for all collected shots as a function of range. Different symbols correspond to different shot lines. Note that the maximum levels monotonically decrease only for the first 3 km in range. They then start increasing again for ranges larger than 3 km, which indicates that the bottom reflected pulse dominates over the direct arrival. Solid and dashed lines are the modeled maximum received zero-to-peak sound pressure levels in the zero degree fixed vertical plane.

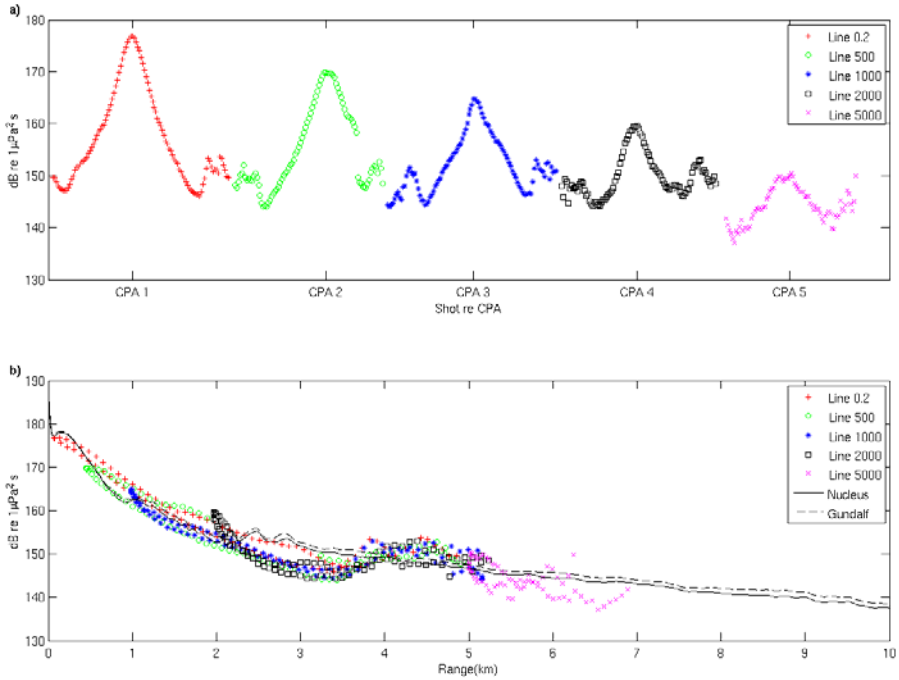

Figure 3.3.7 (a) Maximum sound exposure levels for a 200 ms sliding integration window for each shot plotted relative to the line CPA indicated by the CPA marker on the horizontal axis for each line. (b) Maximum sound exposure levels for a 200 ms sliding integration window for each shot shown for all shots as a function of range. Different symbols correspond to different shot lines. Solid and dashed lines are the modeled maximum sound exposure levels in the zero degree fixed vertical plane.

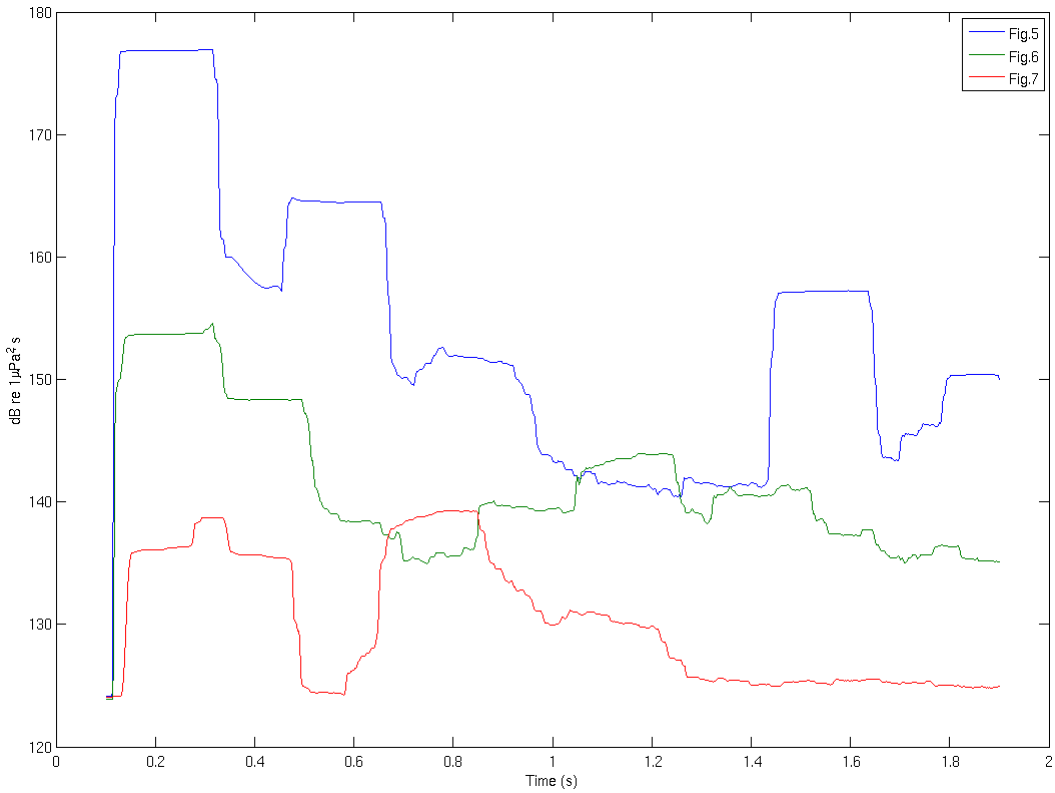

Figure 3.3.8 Sound exposure level vs the temporal position of the center of a 200 ms integration window for the entire shot (including multipath arrivals) for the three shots presented in Figures 3.3.1-3.

first (direct) and the second (bottom reflected) arrivals becomes less than the integration window. The second factor is that the SEL maxima are determined by energy in the multipaths for large range off-axis shots. To support this statement, Figure 3.3.8 shows the SEL for the entire multipath shot as a function of time for the shots shown in Figures 3.3.1–3.

The third attribute used for the recorded data is 1/3-octave band analysis (ANSI/ASA, 2004). 1/3-octave bandwidths are reported to represent the likely lower and upper limits of auditory filters in marine mammal auditory systems for which sparse laboratory bioacoustic data are available (Richardson *et al.*, 1995; Southall *et al.*, 2000; Southall *et al.*, 2003). The results of 1/3-octave band analysis for all collected shots are presented in Figures 3.3.9(a) and 3.3.9(b). The 1/3-octave band received levels are calculated for the entire received signal (2 s temporal window) including all multipath arrivals received over 2 s. Figure 3.3.9(a) shows 1/3-octave band analysis of all shots sequentially plotted both within line number and by line number. Central frequencies of the bands are on the vertical axis. Band numbers 11–43 are included. Figure 3.3.9(b) shows 1/3-octave band analysis of shots within a line plotted as a function of range. The panels correspond to lines 0.2, 500, 1000, 2000, and 5000.

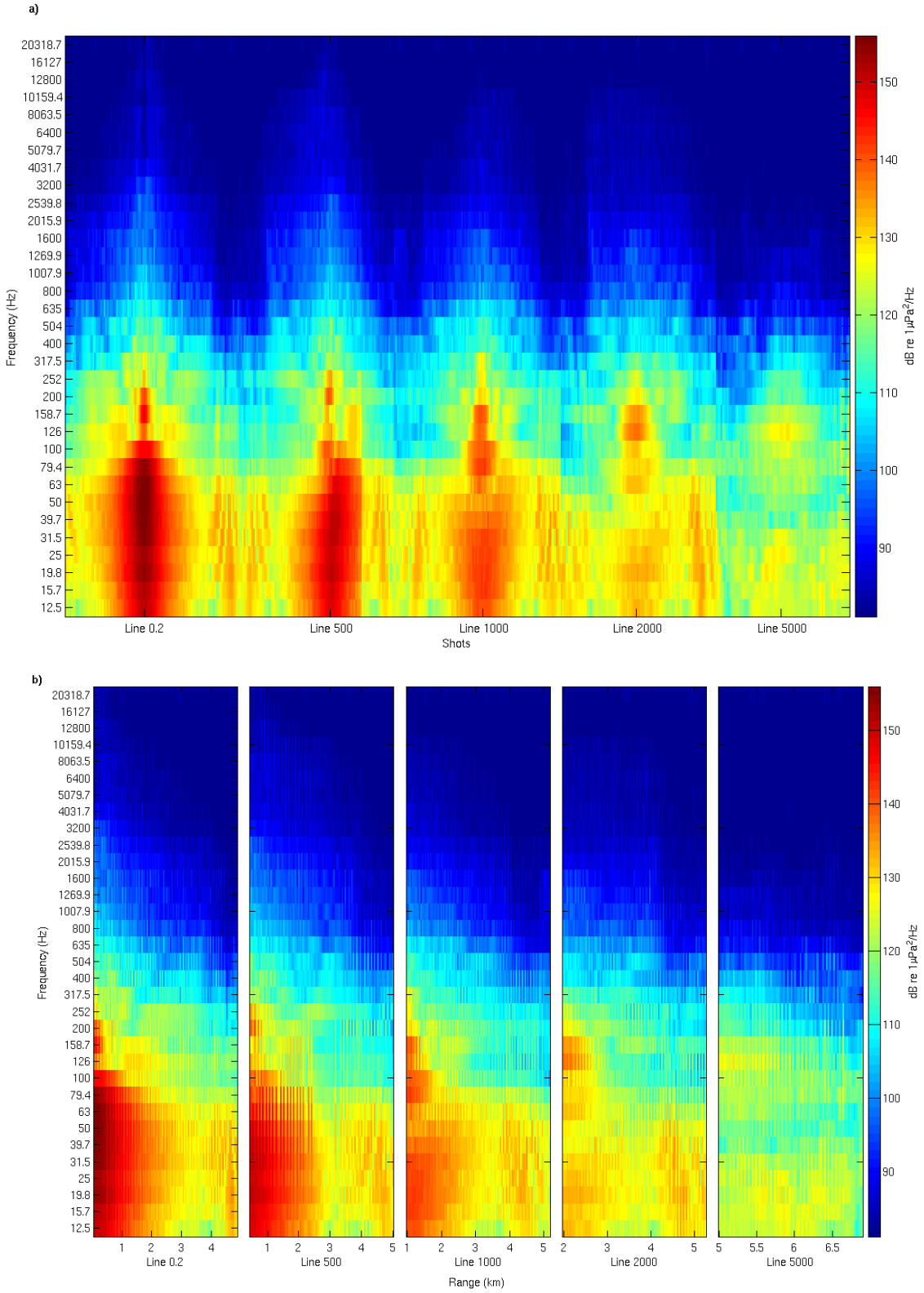

Figure 3.3.9 (a) 1/3-octave band analysis of all shots plotted sequentially both within line number and by line number. Central frequencies of the bands are on the vertical axis and 1/3-octave bands are as defined in ANSI/ASA (2004). Band numbers 11–43 are included. (b) 1/3-octave band analysis of shots within a line plotted as a function of range. The panels correspond to lines 0.2, 500, 1000, 2000, and 5000.

3.4 Acoustic modeling: methods and results

The seismic source acoustic energy distribution in the ocean depends not only on seismic source parameters but also on the propagation channel. Any meaningful mitigation efforts will be dependent on our ability to model quantitatively the acoustic energy distribution from a given seismic array in a particular ocean waveguide. There are several standard acoustic propagation models available to model sound propagation in range-dependent ocean waveguides: RAM, KRAKEN, UMPE, SWAMP, etc. (Collins, 1993; Porter, 1995; Smith and Tappert, 1993; Sidorovskaia, 2004). However, most of the standard models are inherently two dimensional and produce the acoustic pressure distribution of a point harmonic source in the vertical plane of a source and a receiver. There are several issues that have to be addressed when using these models for quantitative modeling of the acoustic pressure distribution from a seismic array: (1) the broadband nature of the seismic pulse produced by each airgun in the array, (2) the complex temporal/angular structure of notional signatures for each airgun in the array due to bubble interactions after firing (Ziolkowski, 1970; Ziolkowski *et al.*, 1982; Laws *et al.*, 1990; Hatton, 2004; Nucleus), and (3) the different ranges to the receiver position for different sources in the array. The last becomes especially important in accounting for the correct relative phases of the high-frequency components at the receiver location. The quality of the calculation will be sensitive to the completeness and accuracy of the parameters describing the propagation channel and the adequacy of notional airgun source signatures to reproduce the near field of the seismic array. The sound speed profile along the propagation path for modeling was derived from expendable bathythermographs and from conductivity-temperature-depth measurements taken during the experiment (see Figure 3.4.1). A very thin surface duct about 10 m thick was present during the experiment. No bottom structure information was collected during the experiment, so the bottom model for the propagation code was based on a historic database (Hamilton, 1980) and previously collected data near the experimental site (Turgut *et al.*, 2002). The bottom model consists of three layers typically present in this area of the Gulf of Mexico: silty clay about 10 m deep, sand deposits up to 1 km deep from the bottom-water interface, and rock formations 1 km below the bottom-water interface.

The calibrated pressure data are modeled using the standard parabolic equation model RAM by Collins (1993), which is upgraded to generate waveguide transfer functions for a broadband multisource array. The measured individual frequency pressure components at the receiver location, $P(f, r_s, z_s)$, are modeled in the frequency domain as

$$P(f, r_s, z_s) = \sum_{i(airguns)} C(f) G(f, r_s, z_s, r_i, z_i) S_i(f), \tag{3.4.1}$$

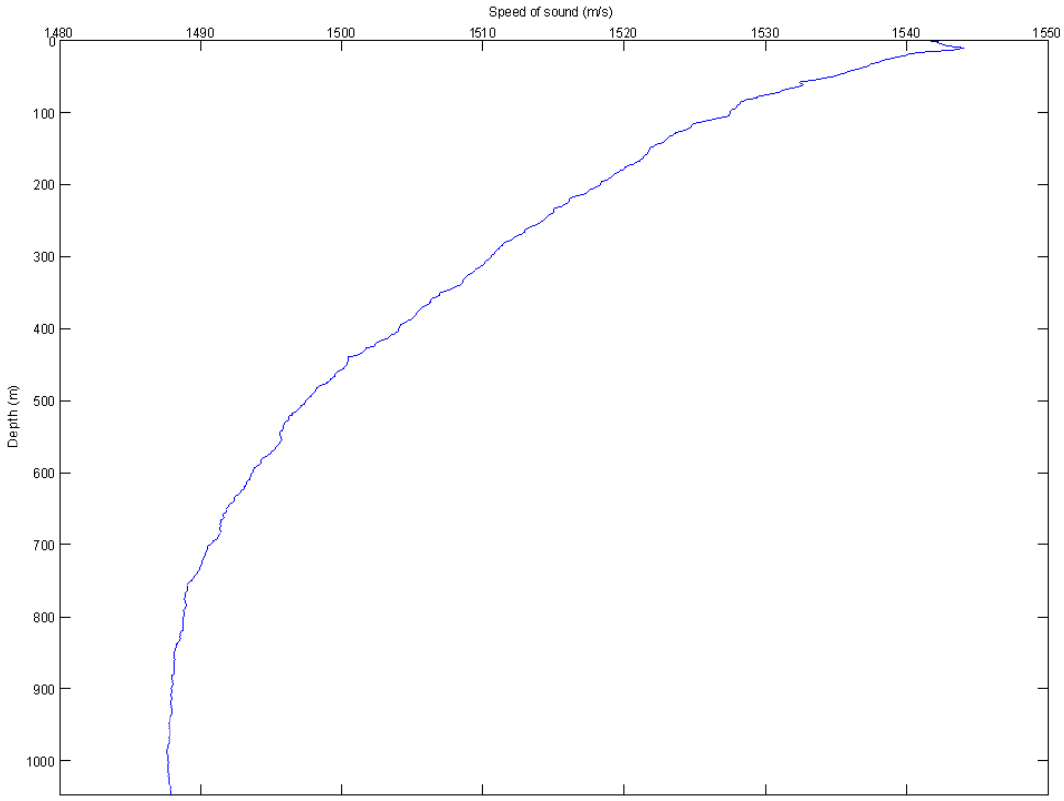

Figure 3.4.1 Sound speed profile in the water column during the experiment. Depth in m is plotted vs sound speed in m/s.

where $G(f, r_s, z_s, r_i, z_i)$ is the complex waveguide transfer function from an individual airgun to the receiver location generated by RAM, $C(f)$ is a highpass filter to cutoff RAM output below 6 Hz and $S_i(f)$ is the Fourier transform of the temporal notional signature of an individual airgun generated by two different airgun characterization models: GUNDALF and NUCLEUS. The waveguide transfer function is generated up to 1000 Hz with a frequency resolution of 0.5 Hz. This frequency resolution provides a sufficiently detailed fine structure for the transfer function to account for the arrival of reflected pulses. The upper frequency is limited by the computational time required by the Parabolic Equation (PE) model to model broadband high-frequency transfer functions for a planar source. Other modeling methods for higher frequencies or a parallel processing approach will be considered to expand the frequency range of modeling in future research. Figures 3.4.2 and 3.4.3 show the transfer function levels (TFL=$10\log\{|G|^2\}$ and arrival phases of two airguns for the closest approach shot on line 0.2 (Figure 3.4.2) and shot 255 on line 500 (Figure 3.4.3), which has a horizontal range of 448 m, a direct distance to the hydrophone of 859 m, an emission angle of 31°, and an azimuthal angle of 260°. The deep minima in Figures 3.4.2 (a) and 3.4.3(a) correspond to the interference structure due to a Lloyd's mirror effect. Analysis of this structure in the measured data allows us to correct the nominal average depth of the airguns in the array from 6 m.

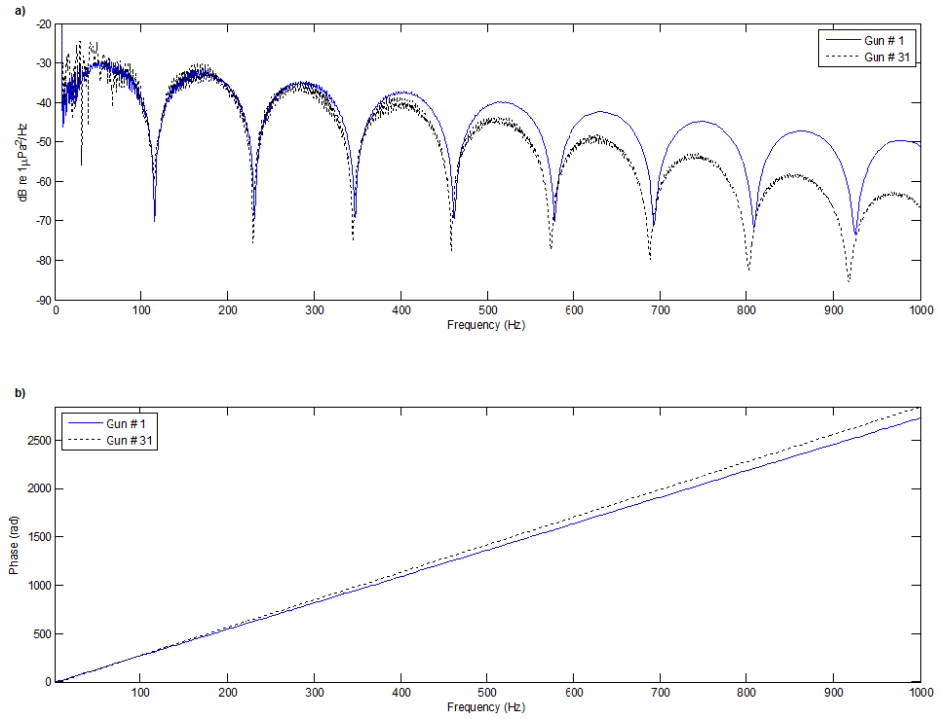

Figure 3.4.2 (a) Modeled waveguide transfer function levels (in dB re 1 μPa^2 /Hz) for airguns 1 and 31 (airgun numbering shown in Figure 3.2.1) for the closest approach shot 249 on line 0.2 [temporal received pressure signature is shown in Figure 3.3.1(a)] vs frequency from 6 to 1000 Hz. (b) The arriving phase for airguns 1 and 31 for the same shot vs frequency. The waveguide transfer functions are generated by the underwater acoustic propagation model RAM adapted to model a broadband planar array of airguns.

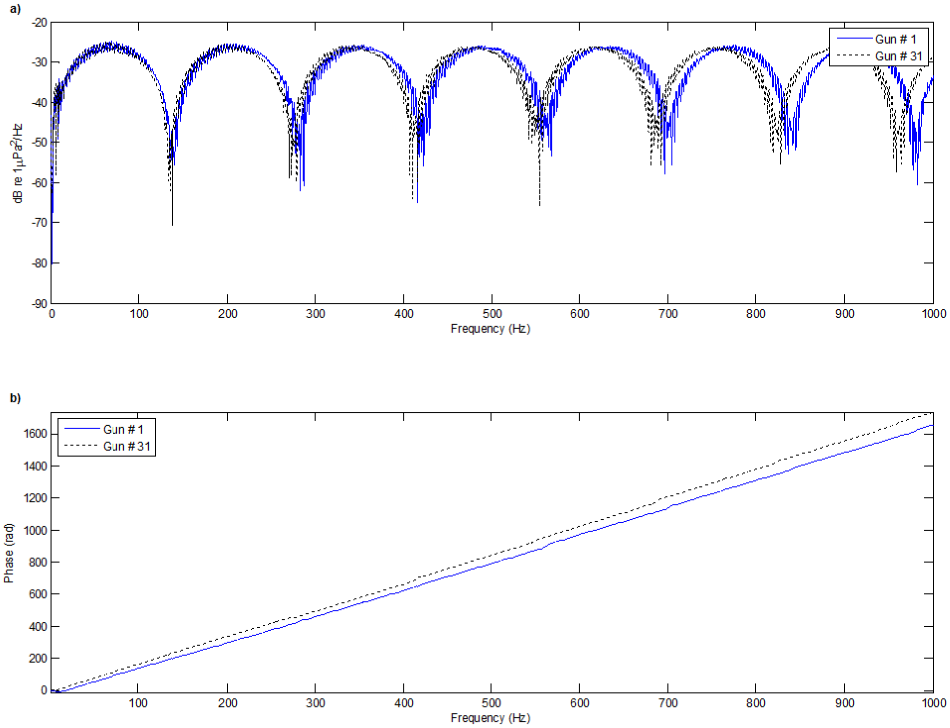

Figure 3.4.3 (a) Modeled waveguide transfer function levels (in dB re 1 μPa^2 /Hz) for airguns 1 and 31 (airgun numbering shown in Figure 3.2.1) for shot 255 on line 500 vs frequency from 6 to 1000 Hz. (b) The arriving phase for airguns 1 and 31 for the same shot vs frequency. The waveguide transfer functions are generated by the underwater acoustic propagation model RAM adapted to model a broadband planar array of airguns.

recorded during the experiment to 6.7 m that is used in modeling. The fine structure of the TFL carries information about reflections from bottom layers and multipaths. The TFL and arriving phase structure indicate that a point source model is not suitable for quantitative prediction of the seismic array energy distribution in the water column.

Figure 3.4.4 shows the temporal notional signatures of selected airguns, which are generated by the NUCLEUS and GUNDALF models, for the seismic array used in the experiment. The notional signature of each airgun in the array is transformed into the frequency domain using a standard fast Fourier transform program and multiplied by RAM generated broadband transfer functions to model the frequency content of the calibrated shots (refer to Eq. 3.4.1). Figures 3.4.5(a) and 3.4.5(b) are a comparison between experimental and simulated data with the source notional signatures generated by GUNDALF and NUCLEUS for the closest approach shot on line 0.2 (a nearly on-axis shot) and for shot 255 online 500 (an off-axis shot). The NUCLEUS model has a high frequency cutoff filter above 800 Hz, so its modeling is only valid up to 800 Hz. GUNDALF is designed to include the high frequency components up to 25 kHz. There are several factors contributing to the discrepancies between experimental and simulated data. The notches in the experimental data near 500 and 750 Hz are most probably due to the first bottom layer reflection that is inadequately specified based on the historical database. Errors in the bottom properties have an effect on the fine structure of the modeled signal. Both airgun modeling codes show better agreement with the experimental data for on-axis shots. The notional signatures used for this calculation were generated and calibrated for on-axis use and so are not the most appropriate for off-axis use (Hatton, 2002).

The Fourier synthesis technique for digitized signals is used to model the time-domain response that was measured in the experiment and used as a starting point for the calculation of the exposure levels in the time domain. Frequencies above 6 Hz are used for comparison with experimental data both because of the rolloff in the receiving system frequency response and because the modeled frequency components at very low frequencies are not considered fully reliable. Figures 3.4.6 (a) and 3.4.6(b) show the quantitative comparison between measured and modeled signatures in the time domain for shot 255 on line 500. SELs over a 200 ms window for the modeled received pulses are also calculated in accordance with Eq. 3.3.5. Figure 3.4.6 (c) shows the comparison of the modeled SEL with one calculated from the experimental data for shot 255 on line 500. The modeled and experimental sound exposure levels agree well for the direct and surface reflected arrivals and the bubble oscillation cycle. The discrepancies between modeled and experimental sound exposure levels for the times corresponding to later arrivals are due to inaccurate information about the bottom structure and for initial times are due to wraparound.

The good agreement between measured and calculated data allows us to model reliably the full three-dimensional acoustic energy distribution from the seismic array in the water column.

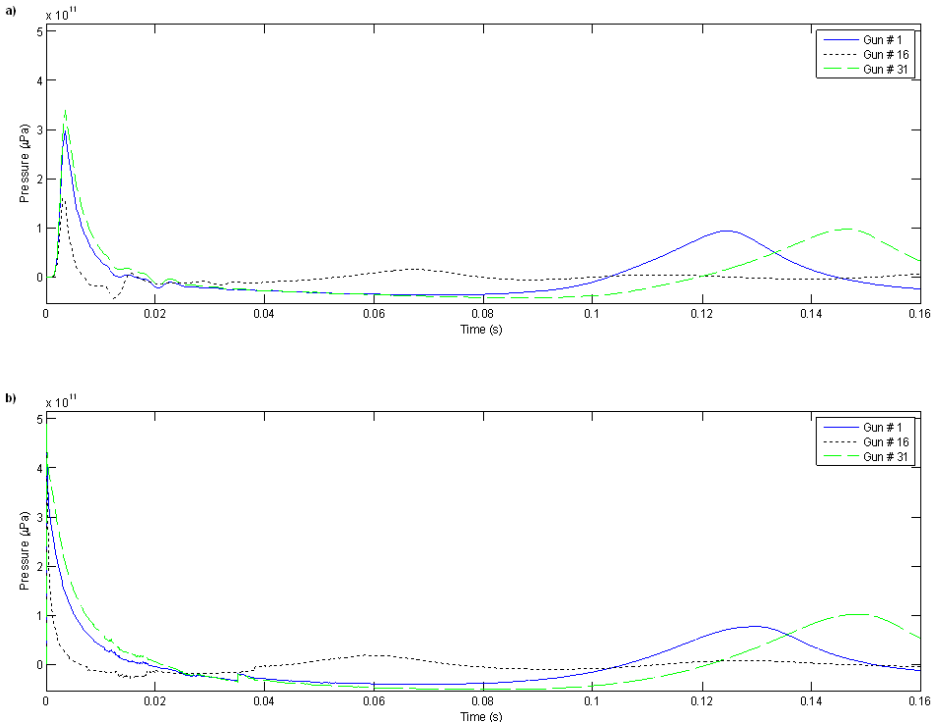

Figure 3.4.4(a) Notional temporal pressure signatures (in μPa) for airguns 1, 16, and 31 (airgun numbering shown in Figure 3.2.1) generated by NUCLEUS vs time in s. (b) Notional temporal pressure signatures (μPa) for the same airguns generated by GUNDALF vs time.

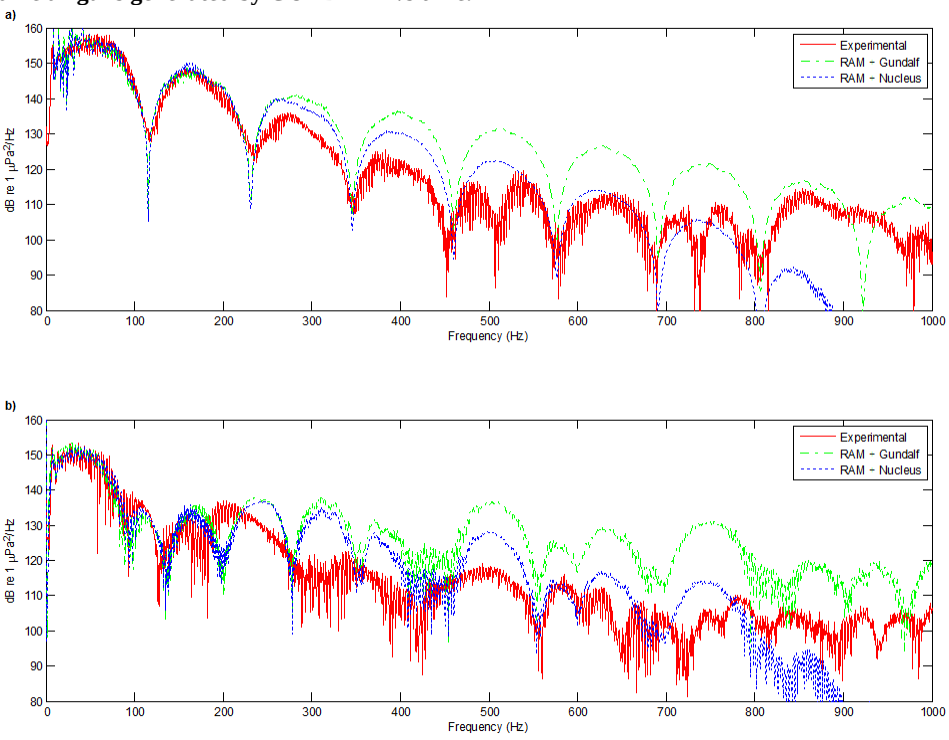

Figure 3.4.5 Spectrum comparison (in dB re 1μPa^2 /Hz) between experimental and modeled data with the source notional signatures generated by GUNDALF and NUCLEUS vs frequency from 6 to 1000 Hz: (a) for the closest approach shot 249 on line 0.2 (nearly on-axis shot) and (b) for shot 255 on line 500 (off-axis shot).

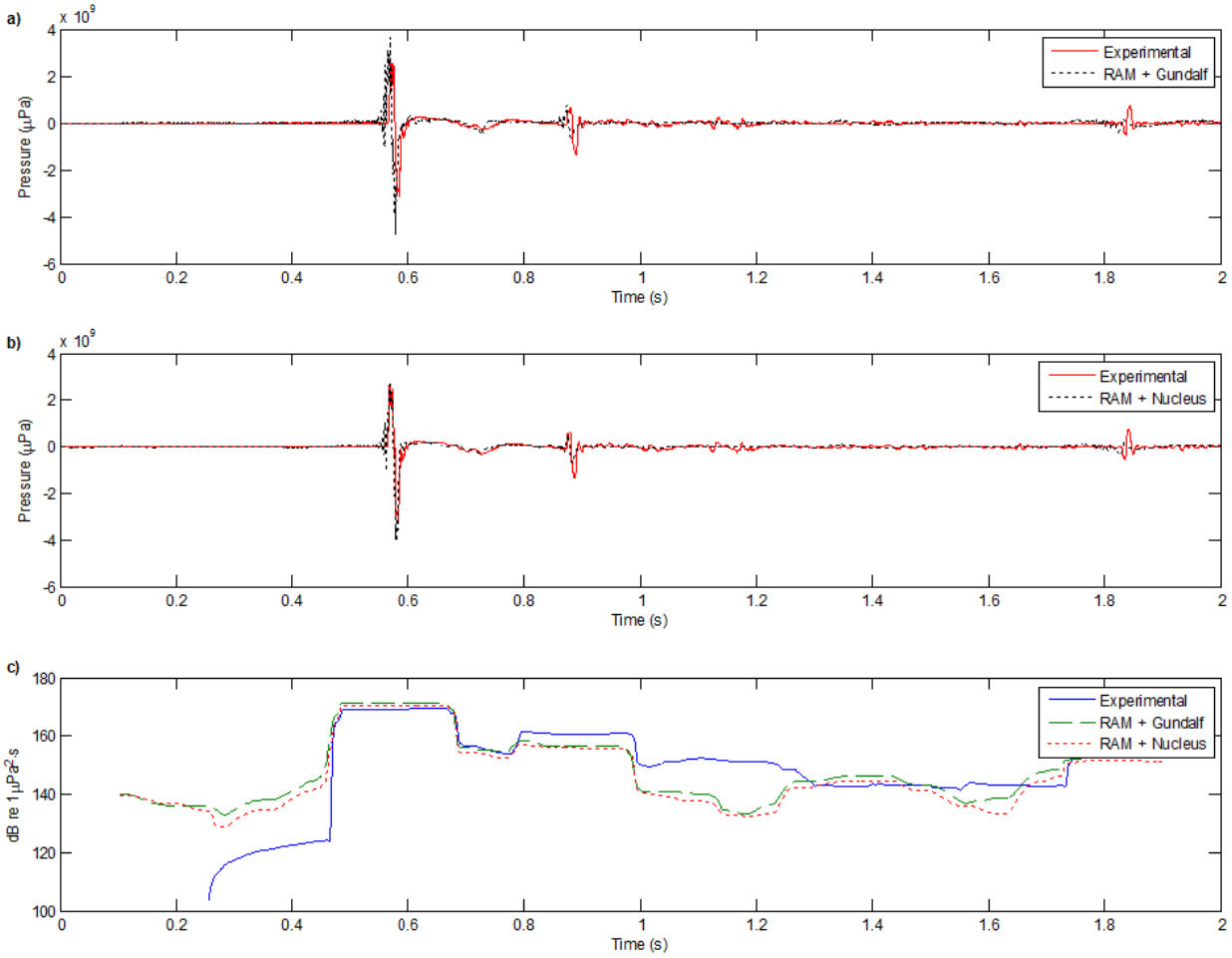

Figure 3.4.6 Comparison between experimental and modeled data (in μPa) vs time in s using frequency components from 6 to 1000 Hz: (a) for shot 255 on line 500 (off-axis shot) simulated with GUNDALF notional signatures, (b) for shot 255 on Line 500 (off-axis shot) simulated with NUCLEUS notional signatures, and (c) sound exposure levels calculated from experimental data and from modeled data for shot 255.

Figure3.4.7 shows the modeled received pressure level as a function of range, depth, and frequency for a point source placed at the center of the array. The power of the point source is equal to the total power of the array used in the experiment. Figures 3.4.8 and 3.4.9 show the modeled received pressure level as a function of range, depth, and frequency in two different vertical planes for the seismic array used in the experiment taking into account the full array geometry and spectral power components of individual array sources extracted from the notional signature frequency components. These characteristics are more meaningful to describe the broadband array radiation field in the waveguide, where array directionality is superimposed on waveguide energy channeling, than the traditional directional pattern of an array in free space. The array acoustic field structure in a waveguide is considerably different from a point source field structure in a waveguide and from the array free-space field. Generation of a series of such maps covering the full frequency band of interest and a set of vertical planes, which allows the generation of three-dimensional SEL maps for a particular array in a particular environment, is the subject of future research.

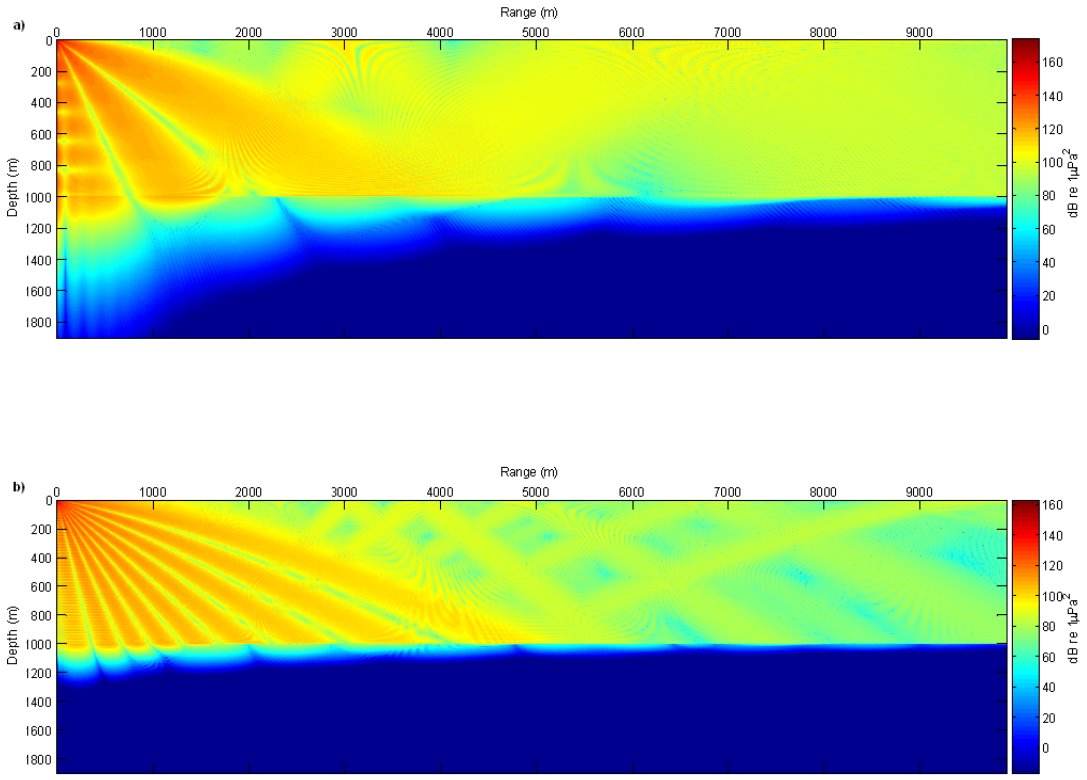

Figure 3.4.7 Modeled received pressure levels in dB re 1 μPa^2 as a function of range from 0.01 to 10 km and depth from 0 to 990 m for a point harmonic source at depth of 6.7 m at (a) 300 Hz and (b) 1000 Hz.

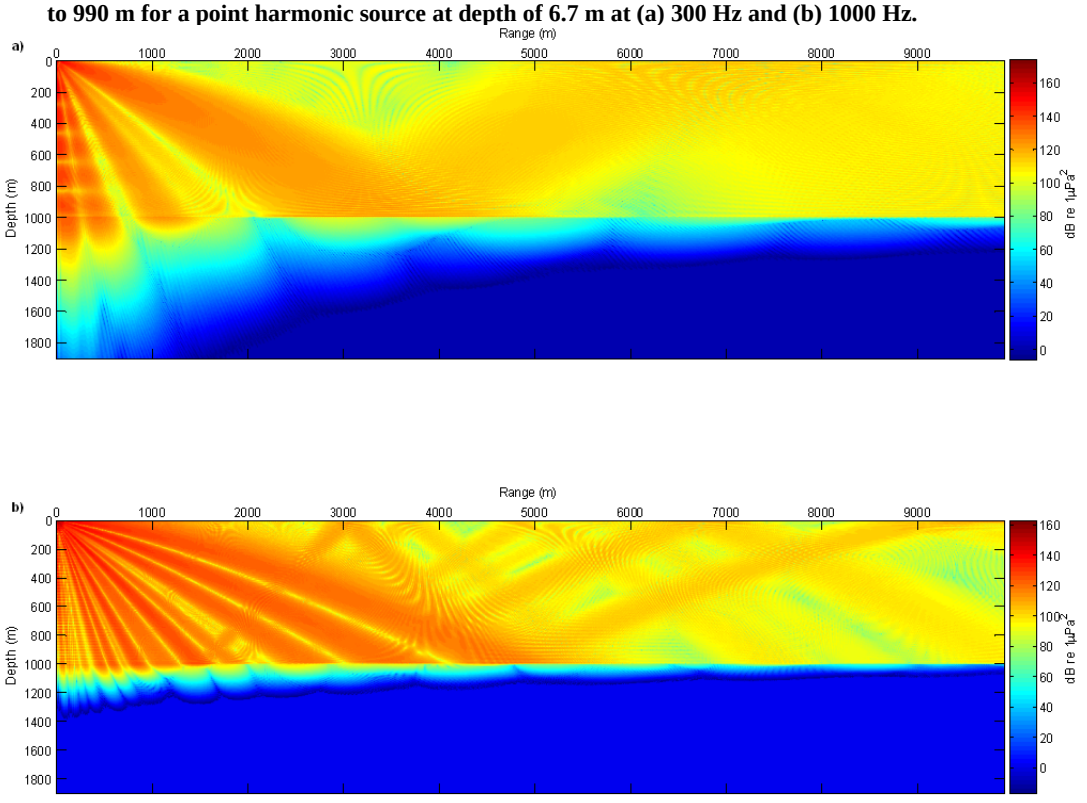

Figure 3.4.8 Modeled received pressure levels in dB re 1 μPa^2 as a function of range from 0.01 to 10 km and depth from 0 to 990 m for the seismic array in the 0°-azimuthal plane (a vertical plane through the central line of the array) at (a) 300 Hz and (b) 1000 Hz.

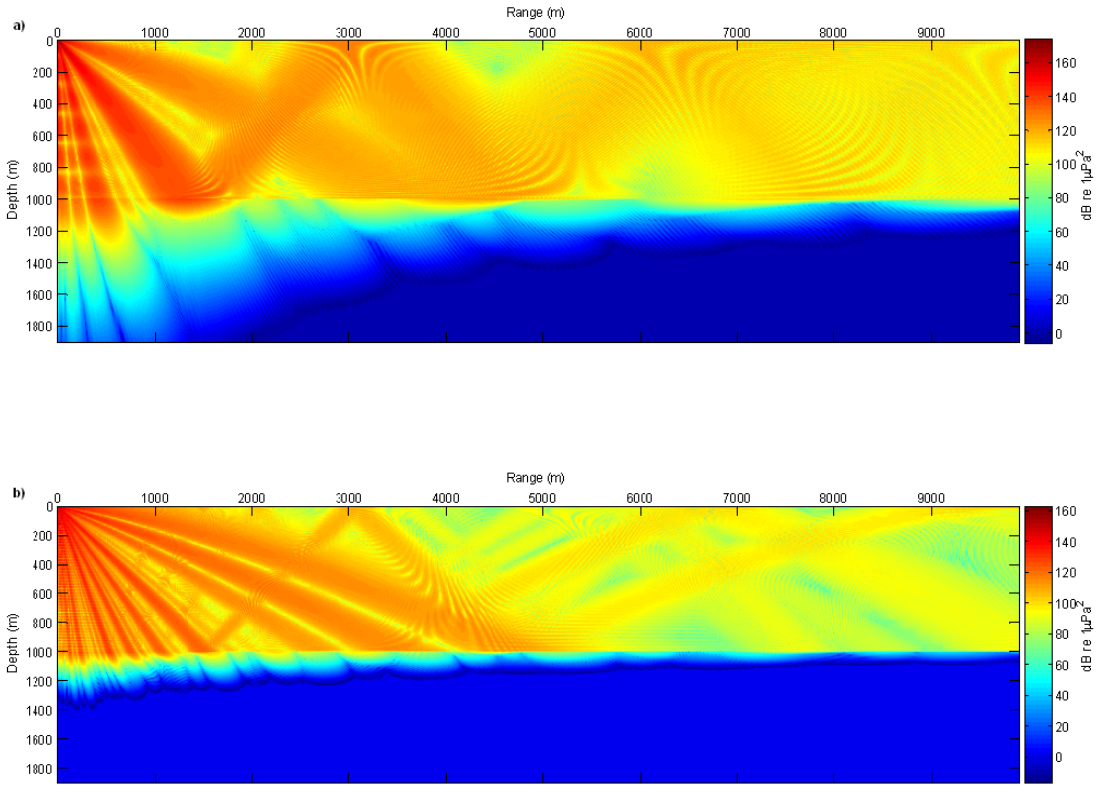

Figure 3.4.9 Modeled received pressure levels in dB re 1 μPa^2 as a function of range from 0.01 to 10 km and depth from 0 to 990 m for the seismic array in the 90°-azimuthal plane (a vertical plane through the array center perpendicular to the travel direction) at (a) 300 Hz and (b) 1000 Hz.

3.5 Discussion and conclusions

The 2003 LADC calibrated data from a typical marine seismic exploration array is a significant contribution to three-dimensional broadband seismic source characterization studies. The data set measures the absolute calibrated pressures for a wide range of angles with frequencies up to 25 kHz. This data set also provides the opportunity to test available modeling tools by quantitative comparison of measured and modeled data. However, the angular/range density of the collected data does not allow detailed testing of the reconstruction of the array directivity for a fixed range or the energy distribution in an arbitrary fixed vertical plane solely based on measured data to compare with modeled results. Additional field data should be collected for validation of the model prediction for a full three-dimensional seismic array characterization. Special attention in future experimental designs should be paid to collecting data for the close-to-horizontal propagation direction that can be critical in studying the issue of energy capture in a near-surface duct. Moreover, the arrival ranges should be extended to address waveguide acoustic propagation issues, such as the existence of convergence and shadow zones and surface duct effects. For example, the number of acoustic precursors formed by the surface duct will be dependent on the range (Sidorovskaia, 2004).

Propagation codes combined with notional signature models predict the broadband data reasonably well. All presented modeling results are *ab initio* calculations with no adjustable parameters. The accuracy of prediction is limited by uncertainties in environmental information and by the accuracy of the source models. Modeling is a useful tool in the prediction of the three-dimensional acoustic energy distribution in an ocean volume of interest. It can be used to determine three-dimensional acoustic energy distribution variations due to anticipated changes in the details of future surveys including changes in ocean environmental conditions and source configuration, without necessarily conducting field experiments. Modeling allows a fairly accurate prediction of sound exposure levels for marine mammals to aid in planning future seismic surveys.

3.6 Acknowledgements

This research has been funded by the Industry Research Funding Coalition through the International Association of Geophysical Contractors and the Joint Industry Project through the International Association of Oil and Gas Producers. We would like to thank Phil Fontana of Veritas for supplying the source notional signatures from GUNDALF and NUCLEUS. GUNDALF is a product of Oakwood Computing, Limited, and NUCLEUS is by PGS. We are grateful to Phil Fontana, Les Hatton of Oakwood Computing, colleagues from the University of Southern Mississippi, particularly Grayson Rayborn and James Stephens and students Chris Walker and Ben Brack, and members of the Industry Research Funding Coalition for helpful discussions. We would like to thank the anonymous reviewers for the valuable comments that helped to improve this published paper. In particular, we would like to express special thanks to one of them, whose insightful suggestions on the interpretation of experimental data, added scientific value to this publication.

Chapter 4 Experimental Design for Measurements to Characterize the 3-D Primary Acoustic Field of a Seismic Airgun Array

The initial requirement for the experimental design for measurements to characterize the 3-D acoustic field of a seismic airgun array was the ability to conduct the experiment during a standard marine seismic exploration survey in the Gulf of Mexico, avoiding as much interference with the survey as possible. During a standard exploration survey, special marine vehicles with attached seismic energy sources, i.e., air gun arrays, and long strings of receiving hydrophones travel along long parallel equally spaced (160 m separation distance) tracks as shown in Figure 4.1 Seismic shots are fired every 25 m along the line. Environmental Acoustic Recording System (EARS) buoys with attached hydrophones were planned to be deployed at some selected positions in the exploration field to collect sufficient acoustic data to characterize the acoustic emission field of the air gun array.

Based on the configuration of available equipment on the marine vessel, the seismic source can either operate in a single shot regime or do flip-flop shooting during which it engages one of the two available air gun arrays (separated by 30 m) while the other array is in an air recharge mode. The configuration for the standard flip-flop operation mode is given in Figure 4.2.

Since the main criterion for experimental design is the three-dimensional characterization of the air gun array acoustic field, appropriate spherical polar coordinates (shown in Figure 4.3) are used for describing the relative positions of the receiving hydrophones of the EARS buoys and the seismic source. The origin of the coordinate system is located at the geometrical center of the air gun array. The azimuthal angle is measured clockwise from the source carrier sailing direction as seen from above. The emission angle, according to present standards in the oil industry, is measured from zero pointing straight down from the air gun array center to 90 degrees in the horizontal plane.

The position of each individual shot is projected to the unit sphere of a receiving EARS hydrophone (Figure 4.4). Projections of all collected shots from all deployed EARS hydrophones are traced back onto unit sphere of the air gun array (Figure 4.5), and the collected information is used for analysis of the field.

Due to variations in temperature, density, and salinity of the waters of Gulf of Mexico, the sound speed in the water column is a function of depth. Therefore the emitted acoustic energy does not travel straight paths, and it is necessary to incorporate into the experimental design and post-experimental data processing, corrections due to refraction in the water column. Simple ray tracing based on Snell's law (Kinsler *et al.*, 1982) is used (Figure 4.6).

The ray tracing algorithm is implemented in MATLAB software, which is optimized for matrix calculations. According to Snell's law:

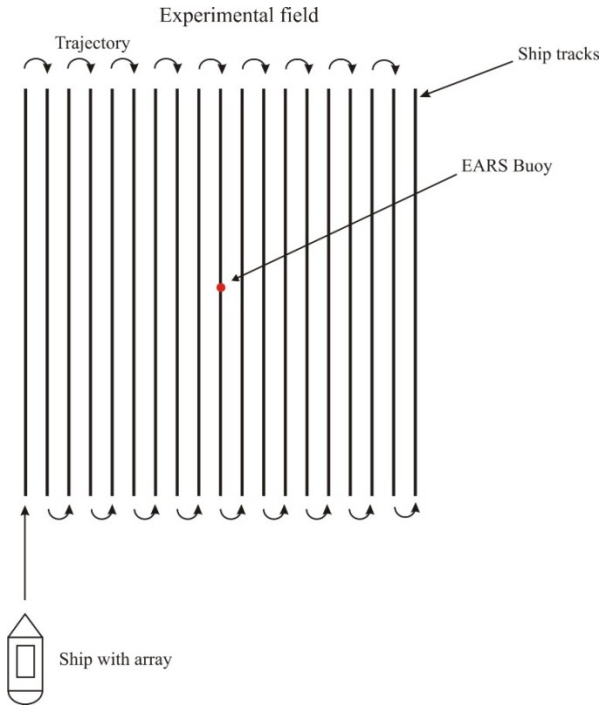

Figure 4.1 Experimental field configuration

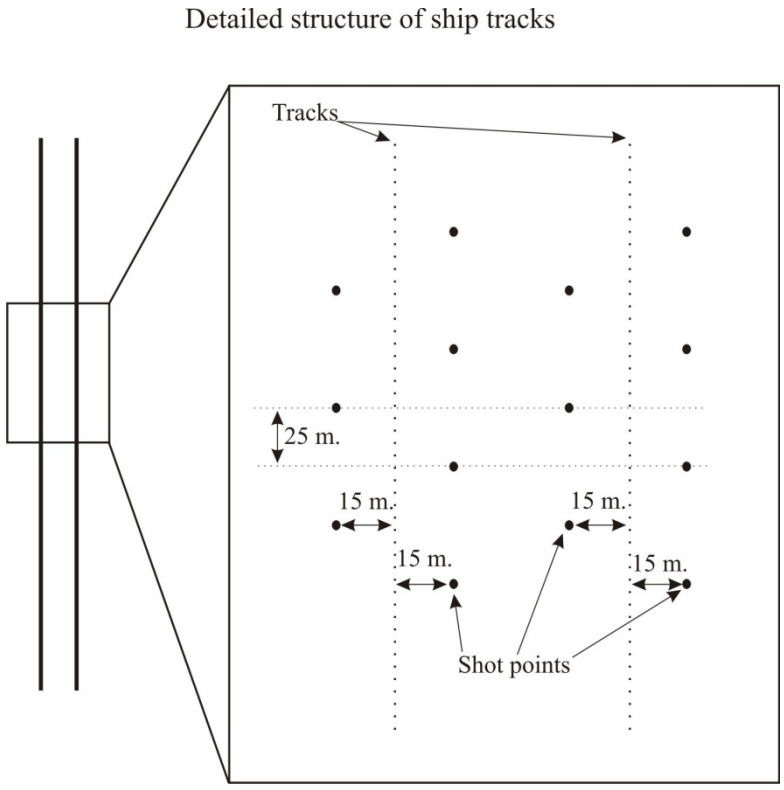

Figure 4.2 Detailed structure of the ship tracks and shots

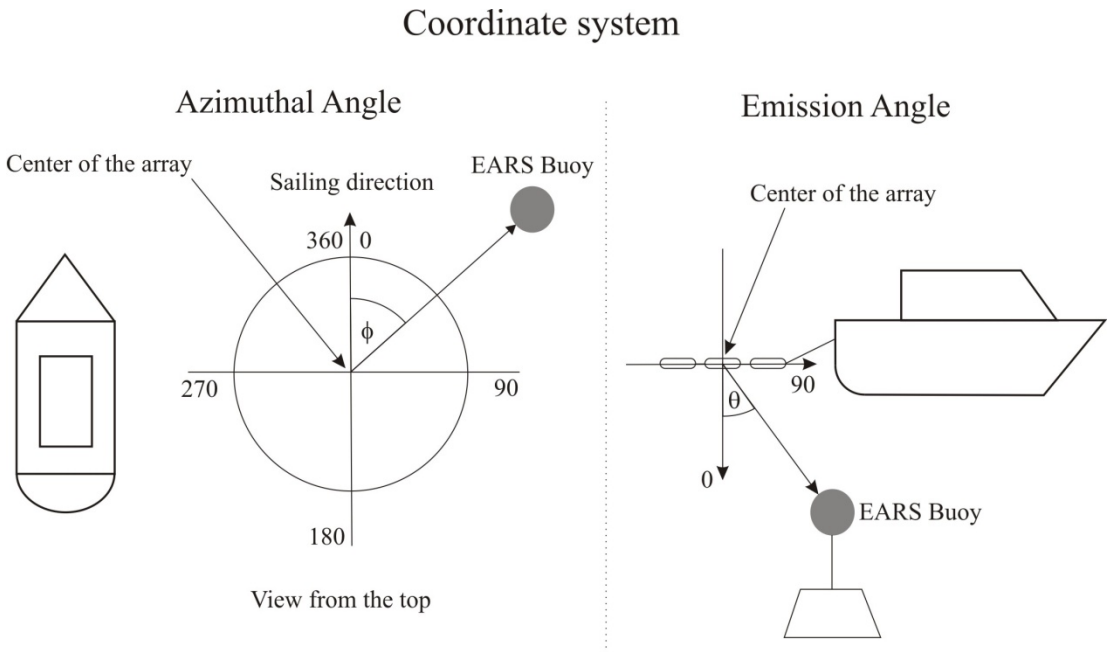

Figure 4.3 Source array coordinate system

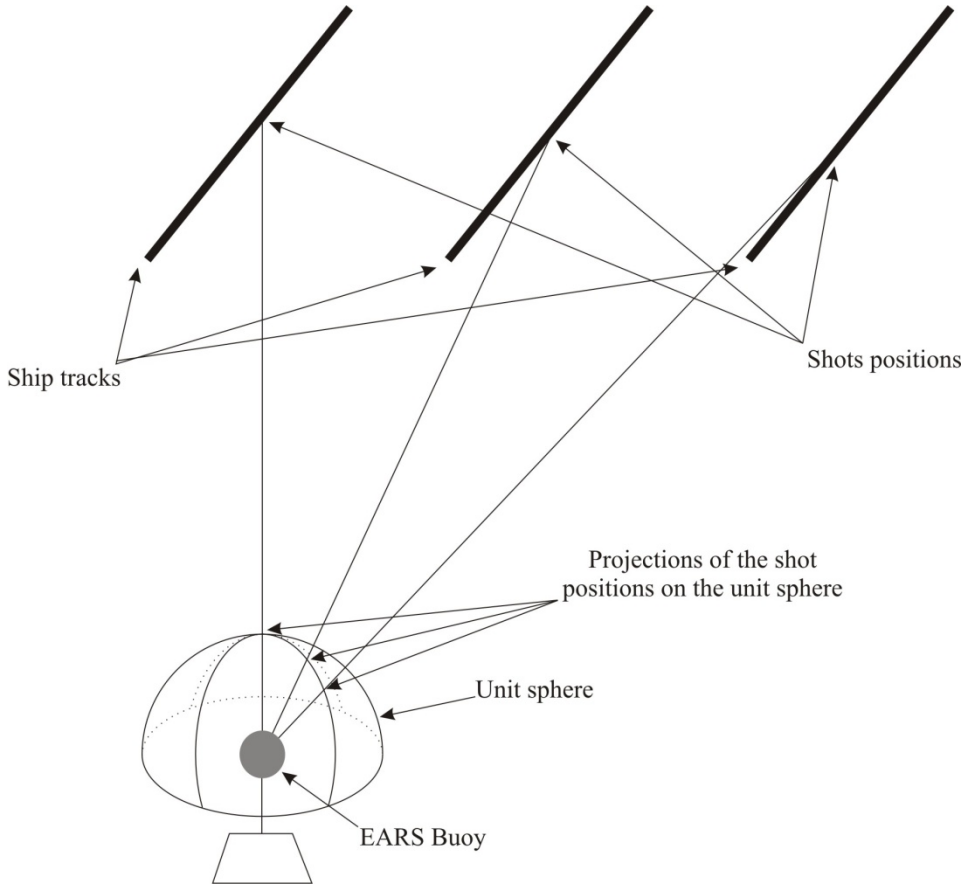

Figure 4.4 Receiving hydrophone unit sphere

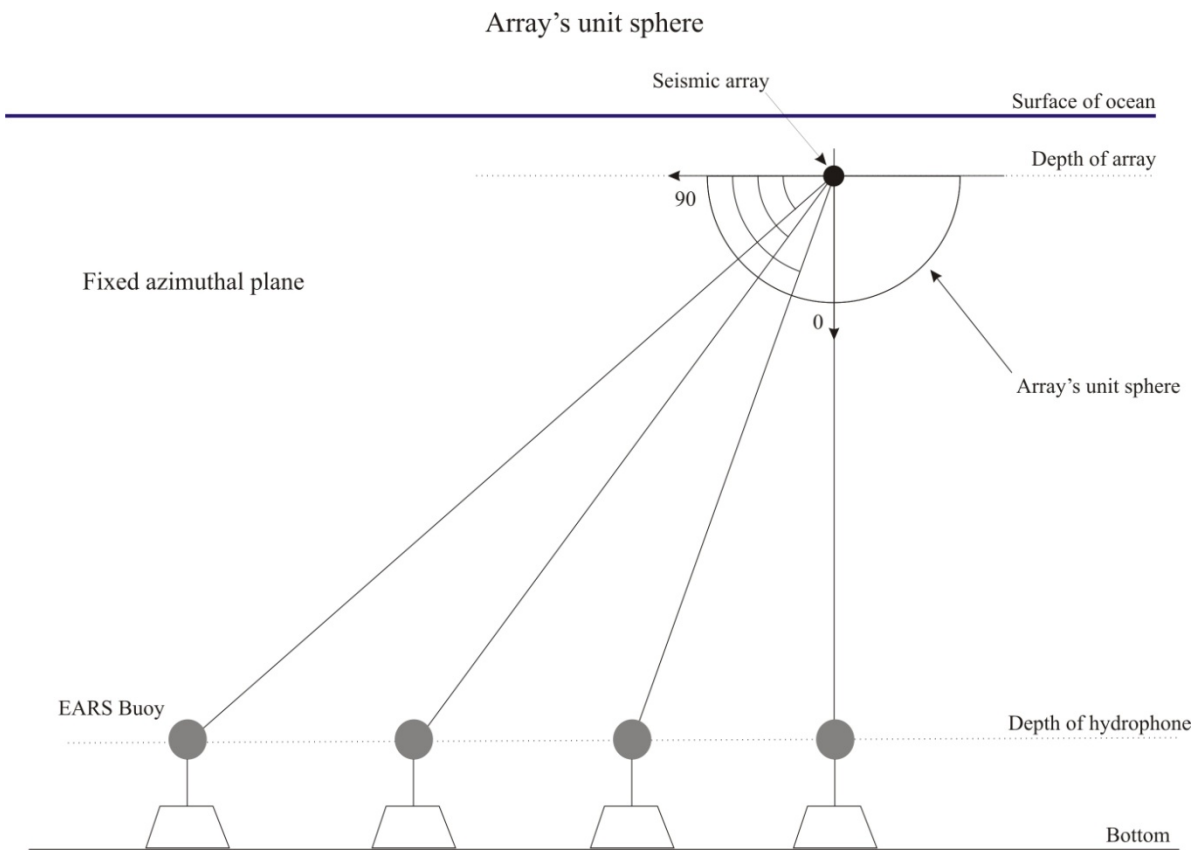

Figure 4.5 Source array unit sphere

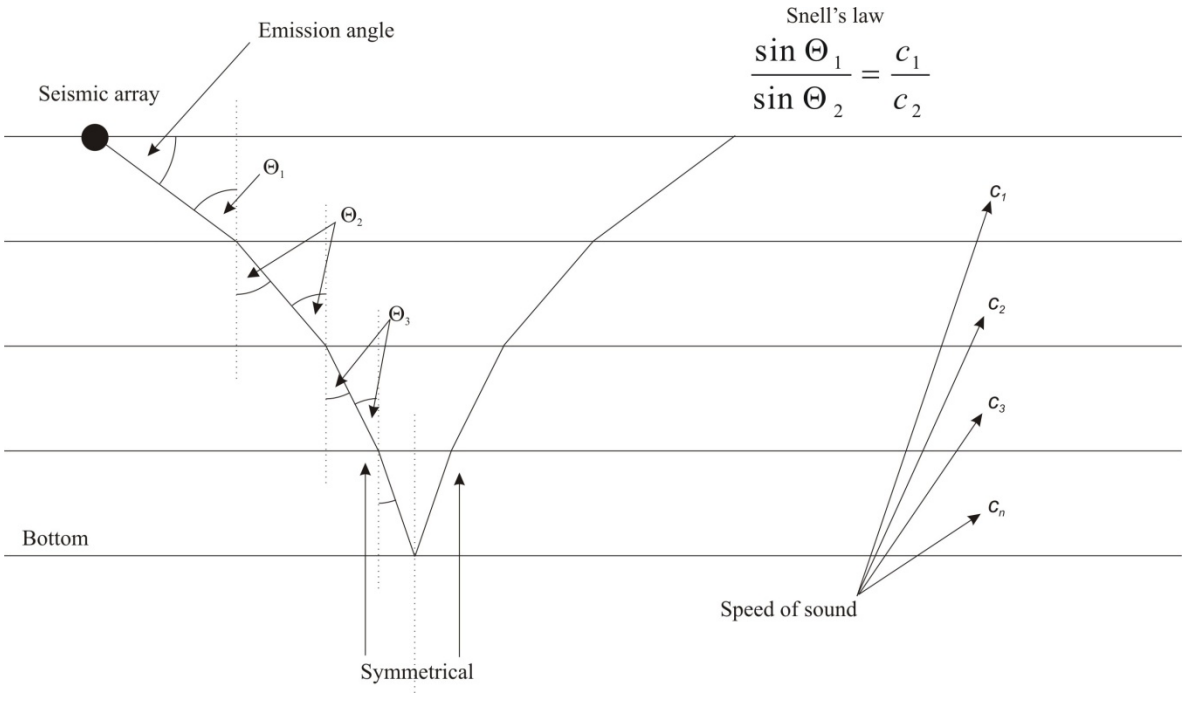

Figure 4.6 Ray tracing

$$\frac{\sin(\theta_{incident})}{\sin(\theta_{refracted})} = \frac{v_{incident}}{v_{refracted}} \tag{4.1}$$

or

$$\theta_{refracted} = \text{asin}\left(\frac{v_{refracted}}{v_{incident}} \times \sin(\theta_{incident})\right). \tag{4.2}$$

In matrix notation it is:

$$[\theta]_{m\times n} = \begin{bmatrix} [\vartheta]_{n\times 1}{}' \\ \text{asin}\left(\begin{bmatrix} S_2 \\ \vdots \\ S_m \end{bmatrix} \times \frac{\sin([\vartheta]_{n\times 1})}{[S_1]}\right) \end{bmatrix}, \tag{4.3}$$

$$m = \frac{z_{bottom} - z_{source}}{\Delta z}, n = \frac{\vartheta_{maximum} - \vartheta_{minimum}}{\Delta\vartheta}, \tag{4.4}$$

where z_{bottom}= depth of the bottom, z_{source}= depth of the acoustic source, Δz = selected depth step, $\vartheta_{maximum}$= maximum ray emission angle, $\vartheta_{minimum}$= minimum ray emission angle, $\Delta\vartheta$ = selected emission angle step, $[\vartheta]_{n\times 1}$= initial ray emission angle vector, $[S]_{m\times 1}$= sound speed vector. Matrix $[\theta]_{m\times n}$consists of the ray angles for all depths from the depth of the source to the depth of the bottom. From this matrix, the horizontal range, which the emitted rays travel from the source to the receiver, is equal to:

$$[Range]_{m\times n} = \begin{bmatrix} [0]_{1\times n} \\ \sum_{k=1}^{i}\left[\tan([\theta]_{(m-1)\times n}) \times \Delta z\right] \end{bmatrix}, \tag{4.5}$$

where i = row number.

The distance traveled along the ray and the travel time are equal to:

$$[Distance]_{m\times n} = \begin{bmatrix} [0]_{1\times n} \\ \sum_{k=1}^{i}\left[\frac{\Delta z}{\cos([\theta]_{(m-1)\times n})}\right] \end{bmatrix}, \tag{4.6}$$

$$[Time]_{m\times n} = \begin{bmatrix} [0]_{1\times n} \\ \sum_{k=1}^{i}\left[\left(\frac{\Delta z}{\cos([\theta]_{(m-1)\times n})}\right) ./ \left([S]_{(m-1)\times 1} \times [0]_{1\times n}\right)\right] \end{bmatrix}. \tag{4.7}$$

By comparing the horizontal range between the location of the source ship and the location of the deployed buoy with the range matrix values, emission angles can be found for given depth of the receiving hydrophone. The bisection algorithm is then used to find the ray emission angle, the distance traveled along the ray, and the propagation time for the given relative source-receiver positions. For the bottom reflected rays, the range, distance traveled, and propagation time matrices are:

$$[Range]_{m\times n} = \begin{bmatrix} [0]_{1\times n} \\ \sum_{k=1}^{i} \left[\tan([\theta]_{(m-1)\times n}) \times \Delta z\right] \end{bmatrix} + \begin{bmatrix} \sum_{k=i}^{n} \left[\tan([\theta]_{(m-1)\times n}) \times \Delta z\right] \\ [0]_{1\times n} \end{bmatrix}, \quad (4.8)$$

$$[Distance]_{m\times n} = \begin{bmatrix} [0]_{1\times n} \\ \sum_{k=1}^{i} \left[\frac{\Delta z}{\cos([\theta]_{(m-1)\times n})}\right] \end{bmatrix} + \begin{bmatrix} \sum_{k=i}^{n} \left[\frac{\Delta z}{\cos([\theta]_{(m-1)\times n})}\right] \\ [0]_{1\times n} \end{bmatrix}, \quad (4.9)$$

$$[Time]_{m\times n} = \begin{bmatrix} [0]_{1\times n} \\ \sum_{k=1}^{i} \left[\frac{\left(\frac{\Delta z}{\cos([\theta]_{(m-1)\times n})}\right)}{([S]_{(m-1)\times 1} \times [0]_{1\times n})}\right] \end{bmatrix} + \begin{bmatrix} \sum_{k=i}^{n} \left[\frac{\left(\frac{\Delta z}{\cos([\theta]_{(m-1)\times n})}\right)}{([S]_{(m-1)\times 1} \times [0]_{1\times n})}\right] \\ [0]_{1\times n} \end{bmatrix} \quad (4.10)$$

As an example and an initial sound speed function, the sound speed profile measured during a previous experiment (Littoral Acoustic Demonstration Center (LADC) 03) in a nearby area is used in the calculations. It is shown in Figure 4.7. The sound speed measured in meters per second is plotted on the horizontal axis and the depth of the water column measured in meters is plotted on the vertical axis. The sound speed profile used for ray generation has a small surface duct, i.e., a small (about 10 m deep) waveguide which traps direct rays emitted at angles beyond 88.9 degrees.

Examples of trajectories of direct rays emitted by the seismic source and bottom reflected rays are shown in Figures 4.8 and 4.9. Range or horizontal distance from the acoustic source measured in meters is plotted on the horizontal scale. The typical seismic source depth during standard exploration surveys is about 6-7 meters.

Emission angles for the generated rays are shown in Figures 4.10 and 4.11. The color bar corresponds to the emission angle in the coordinate system used in the experiment design. The dark red color above the refraction boundary corresponds to the shadow area where no primary arrivals could be received by the receiving hydrophone. Since the main objective of the experiment is to measure the primary emission field of a seismic source, hydrophones located in the dark red area will not record any useful information about the field of interest. This sets a constraint on the location of hydrophones during the experiment. The name primary arrival is given to the combination of the direct arrival and the immediate surface bounce which together form the field of interest for characterizing the airgun array.

Direct and bottom reflected rays (shown in Figure 4.12) are used to generate the time delay between arrivals as a function of the horizontal range and depth of the receiving hydrophone, and are shown in Figure 4.13. The color bar corresponds to time delay measured in milliseconds. The dark blue color corresponds to shadow zones where no primary arrivals are observed on the receiving hydrophones.

Following the example of an acoustic recording from the similar LADC03 experiment shown in Figure 4.14, a decision by the Project Study Group (PSG) was made to establish a constraint on the time

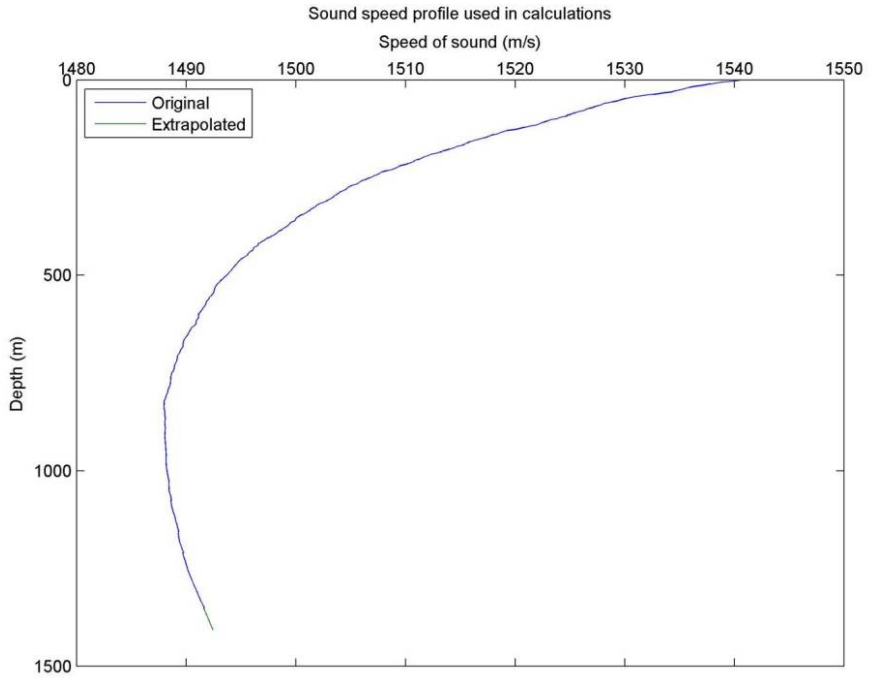

Figure 4.7 Sound speed profile

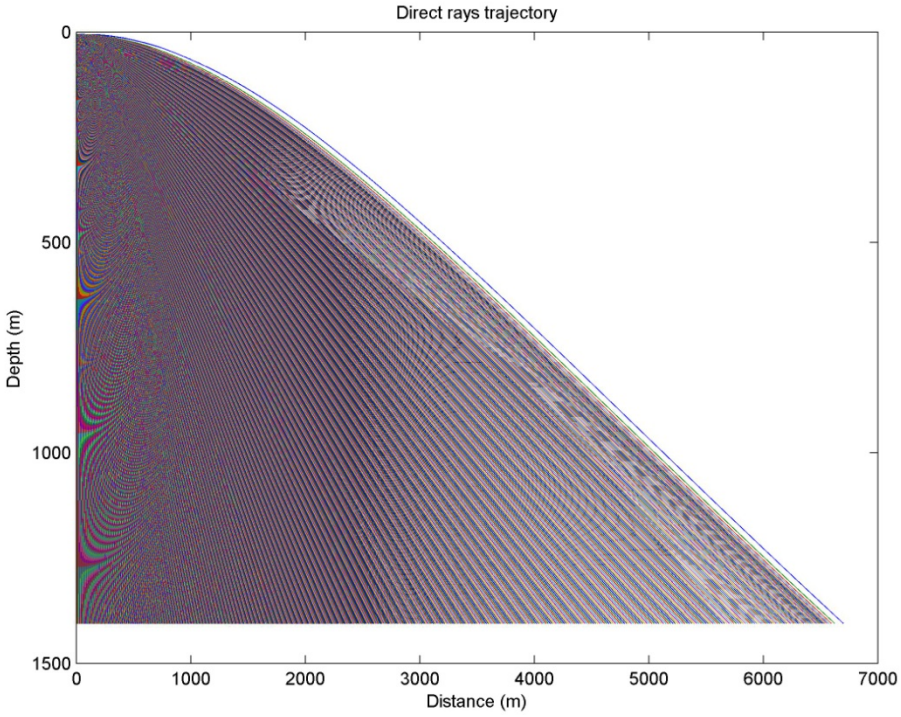

Figure 4.8 Direct emitted rays' trajectories

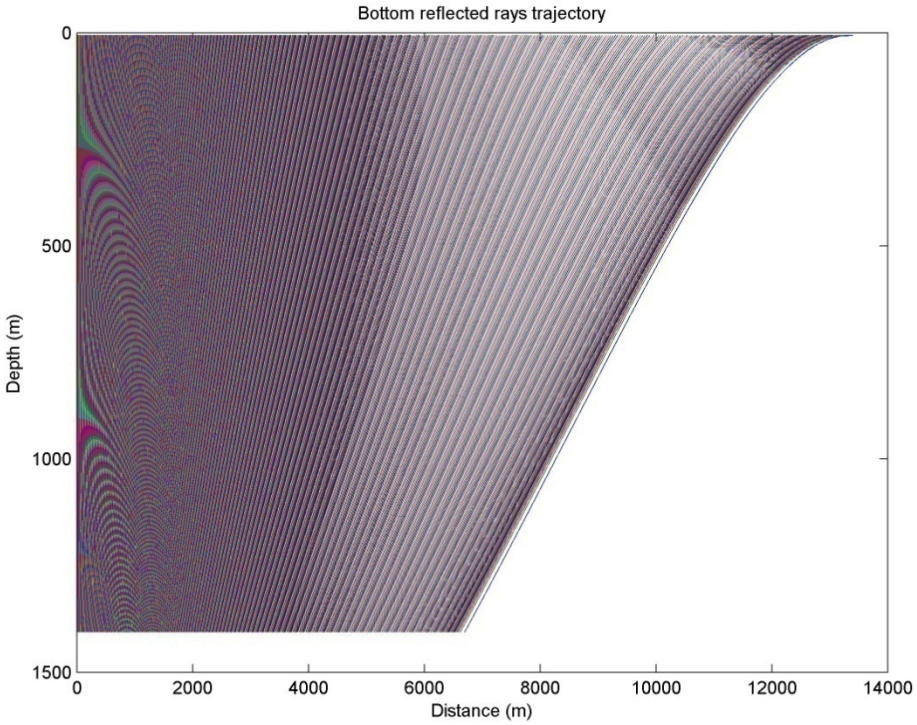

Figure 4.9 Bottom reflected rays' trajectories

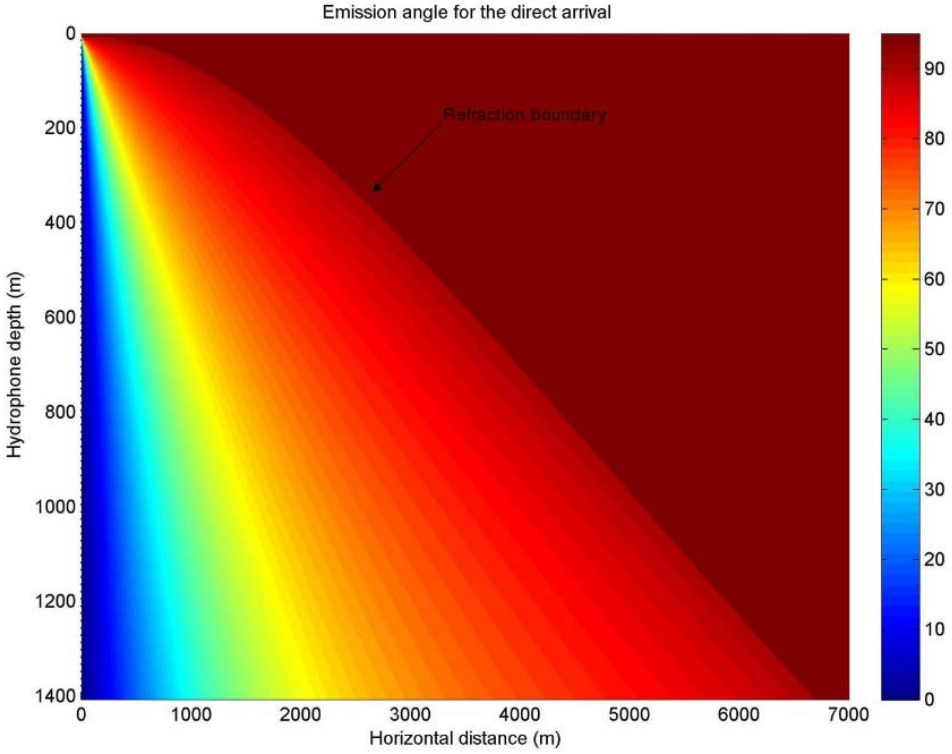

Figure 4.10 Emission angles for direct emitted rays

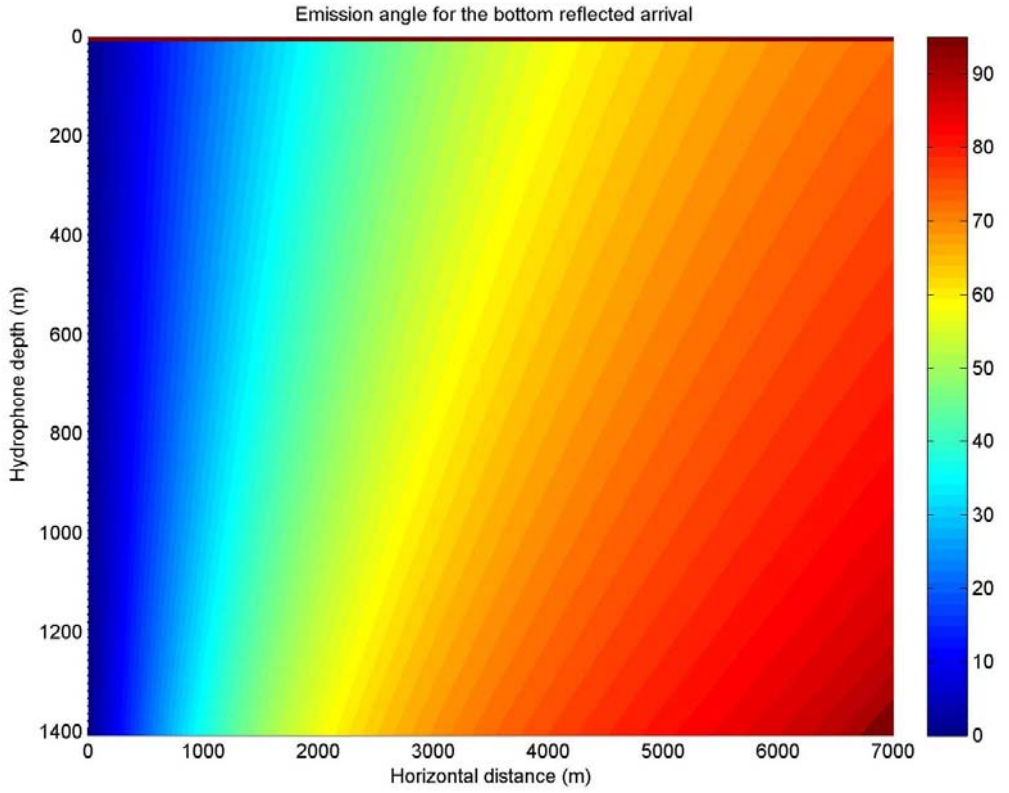

Figure 4.11 Emission angles for bottom reflected rays

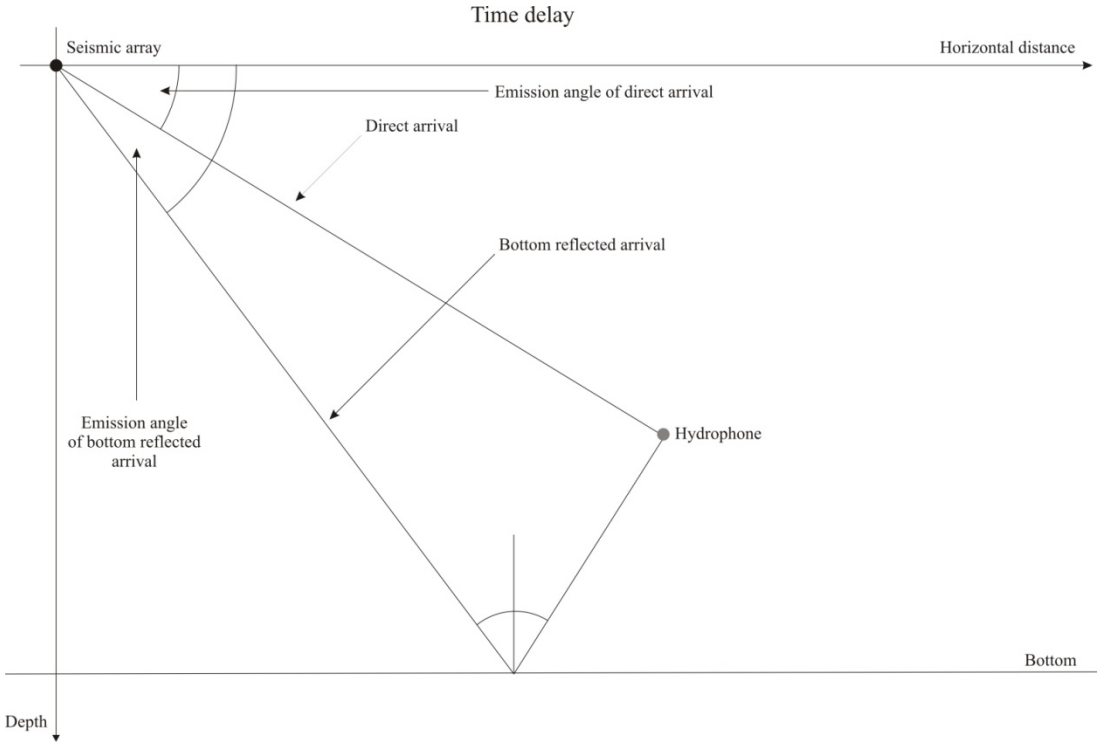

Figure 4.12 Estimation of time delay between arrivals

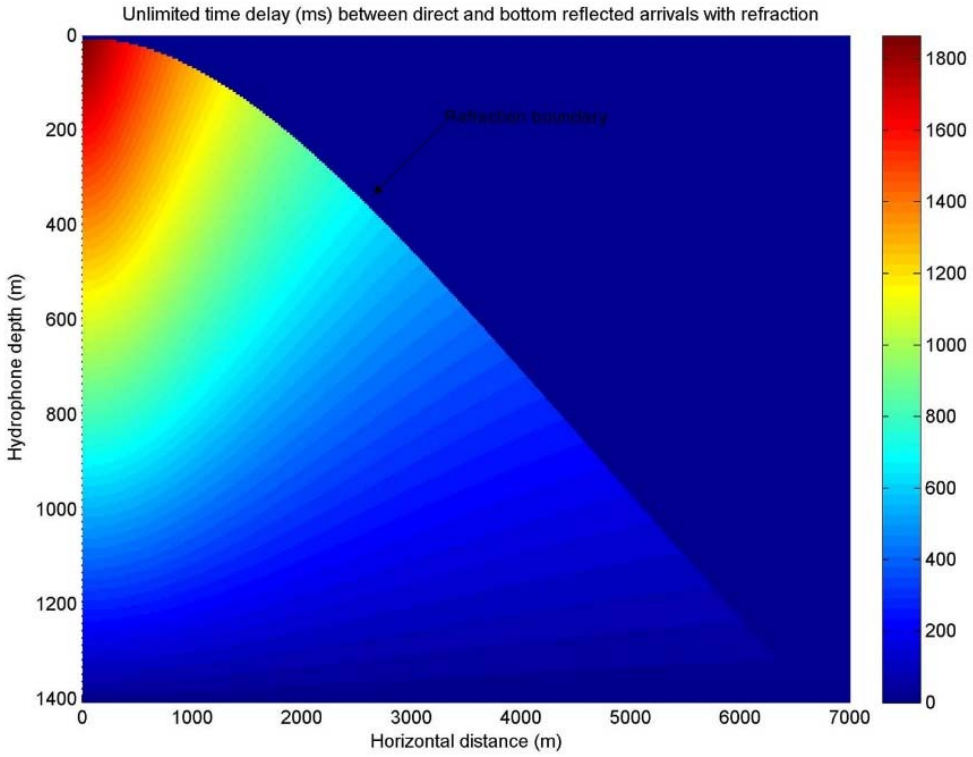

Figure 4.13 Time delays

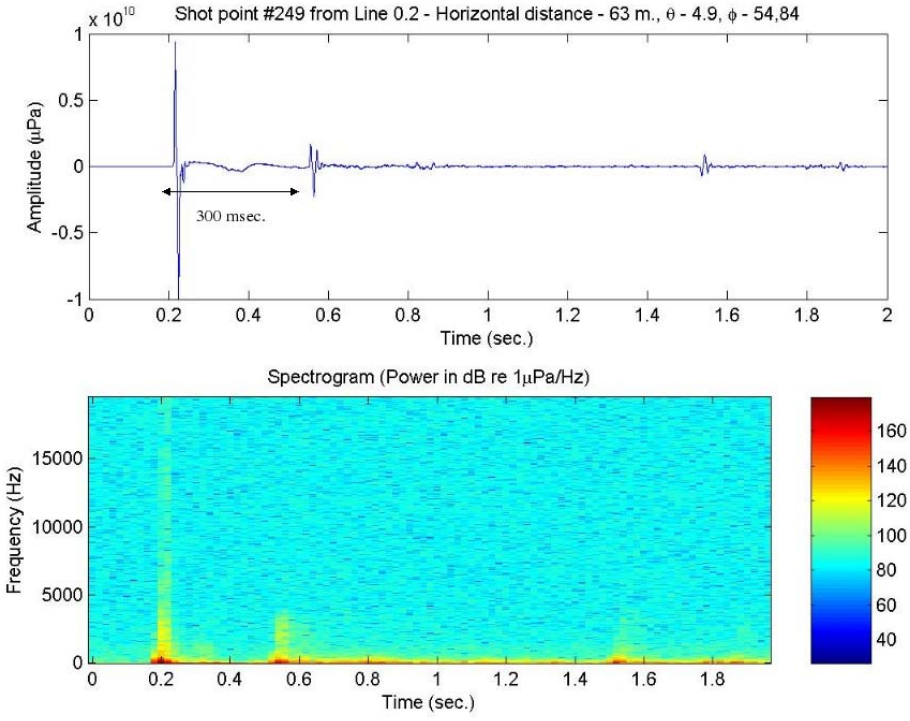

Figure 4.14 Shot example from LADC 2003

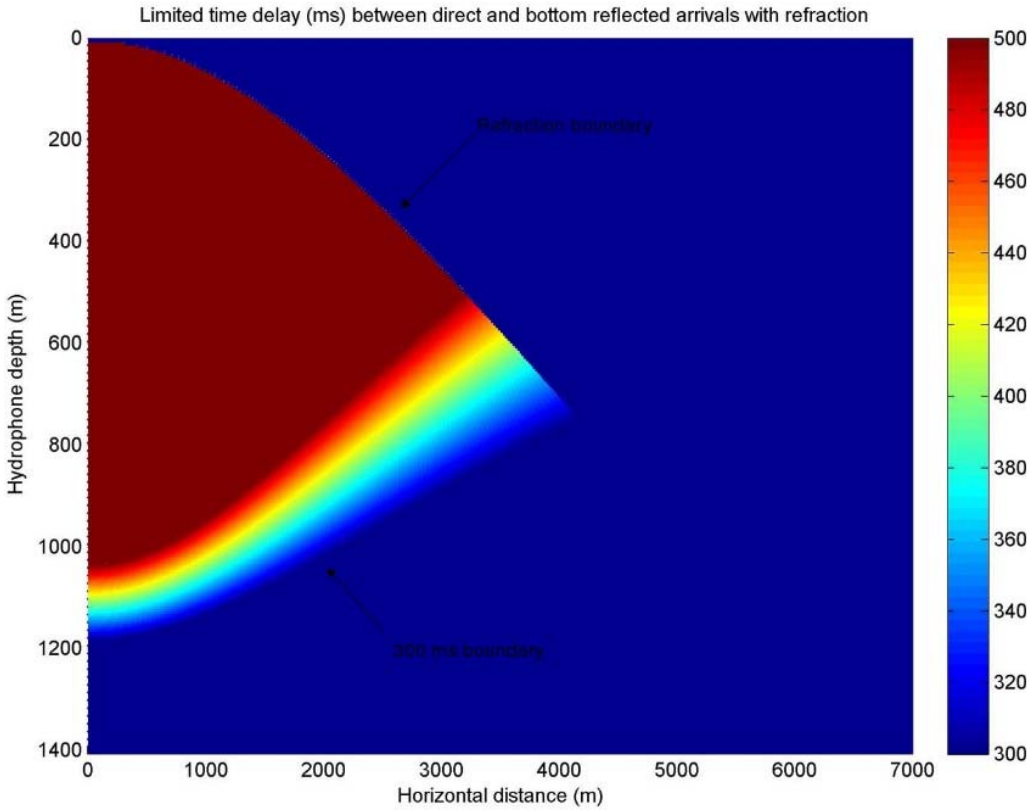

Figure 4.15 Limited time delay between arrivals

separation between primary and bottom-reflected arrivals of at least 300 milliseconds to make it possible to study the bubble oscillation phenomenon. The resulting experimental zone is shown in Figure 4.15, where the dark blue color on the color bar corresponds to the zone of unusable data due to both refraction and time separation constraints. According to Figure 4.15, useful information will be collected on hydrophones deployed at depths up to 1200 meters and located at horizontal ranges from the seismic source up to 4.5 kilometers.

The structure of our long EARS buoy mooring is given in Figure 4.16. It shows a long vertical mooring with flotation, anchor, acoustical releases, and several EARS buoys units, with hydrophones attached through a cabling system. The maximum sampling rate for the current generation of buoys is 200 kHz. Based on that, the buoy can be configured in up to a 4-channel mode giving a sampling rate of at least 50 kHz per channel, collecting data from up to 4 hydrophones simultaneously. In order to investigate the emission field from a seismic source which is relatively strong compared to the usual background noise in close proximity to the source ship, each hydrophone depth is shared between two hydrophones – one sensitive for ambient noise measurement and another one desensitized for measuring the emission field from the nearby seismic source. The dynamic ranges of both hydrophones overlap in such a way that

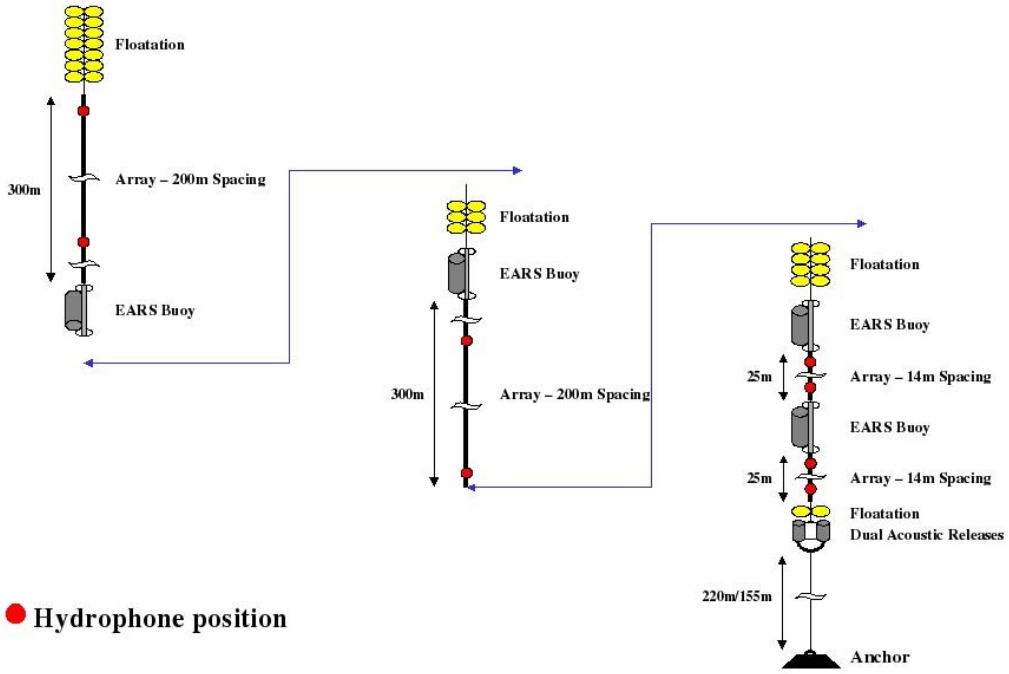

Figure 4.16 EARS buoy configuration

there is the possibility of merging collected data into one single data stream. Based on this, in the 4-channel mode each EARS buoy covers two hydrophone depths. The relative positions of the hydrophone depths can be adjusted by shifting the positions of buoys and cabling systems along the main line. There is a limit on the separations between hydrophones connected to the same buoy due to the length of the available cabling system.

One of the objectives of the experiment was to collect measurements for a large variety of emission and azimuthal angles and distances between the seismic source and receivers. In the initial experimental design, ship tracks were equally spaced, separated by a fixed distance of 160 m. In order to get equal emission angle separation (Figure 4.17), the position of each hydrophone on the mooring string (Figure 4.18) was calculated by using ray tracing. For the proposed configuration: 1) the number of received shots for given azimuthal and emission angles (i.e., a given solid angle); 2) the closest shot travel distance along the emitted ray, for the given solid angle; 3) the covered shot field plots for individual hydrophone depths; and 4) final summations of all received shots are calculated and have been analyzed by the PSG for quality control. To plot three-dimensional distributions, color polar plots are used.

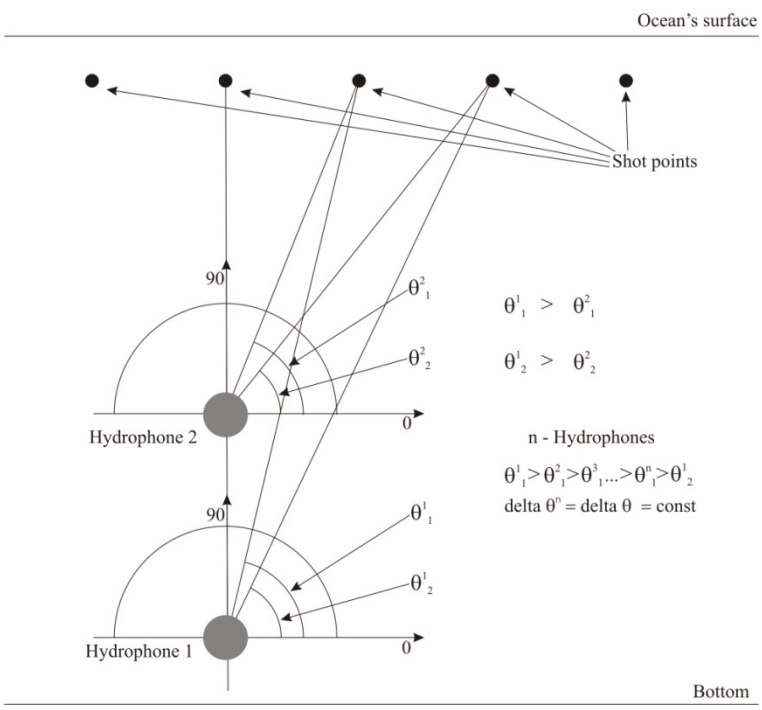

Figure 4.17 Uniform angular filling

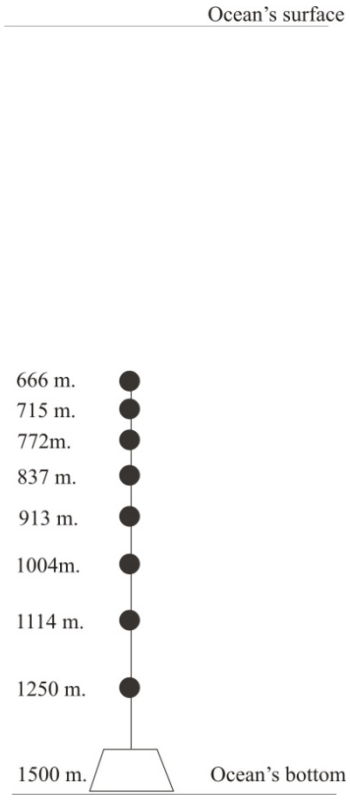

Figure 4.18 Hydrophone string configuration for uniform filling

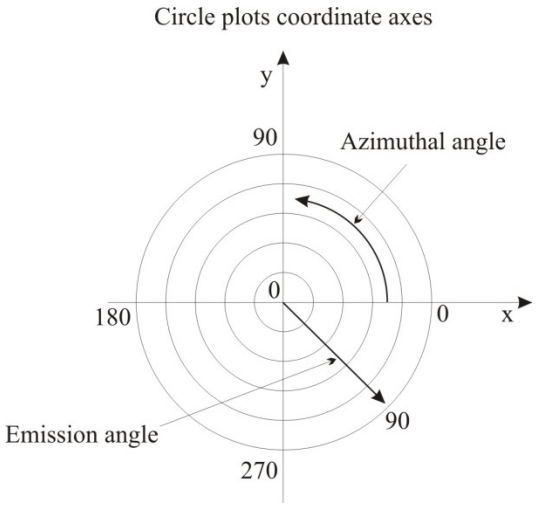

Figure 4.19 Color plots coordinate system

The coordinate system is shown in Figure 4.19. On color polar plots, the emission angle is plotted radially with zero degrees at the center of the figure. This means overhead shots are at the center and near surface arrivals are near 90 degrees on the outer ring. The azimuthal angle is plotted counterclockwise as seen from below the seismic exploration array.

The angular shot density distribution for the initial configuration is shown in Figure 4.20 using the coordinate system described above. The color bar corresponds to the number of shots received according to the simulations for given emission and azimuthal angles. The dark blue color corresponds to emission angles with no data received. After a number of simulations adjusting hydrophone location to try to reduce the dark blue area of no data and due to existing cabling system limitations, a new configuration was proposed (Figure 4.21). The corresponding angular shot density for the arrangements of Figure 4.21 is shown in Figure 4.22. The empty space in the angular shot density distribution is due to the fixed separation between lines and the limited amount of available hydrophones and buoys. To fill in missing data, additional shots were planned to be done by and auxiliary vessel.

The experiment was scheduled to be conducted during the Summer 2005, but due to a mooring breakdown during the equipment deployment onsite, it was rescheduled to a future date. Even without the breakdown, the success of the experiment was problematic due to weather delays in the shooting schedule, since the EARS buoys recorded automatically and could not be delayed.

After investigation of the reasons for the initial experiment failure, and taking into account the importance of this experiment, a new experiment with a dedicated source vessel was proposed to the PSG. This time the source vessel towing the air gun array would follow an optimal path determined from experiment simulations and our experience from the initial experiment design. This allowed variations of line lengths and spacing between lines in addition to variations in hydrophones depths.

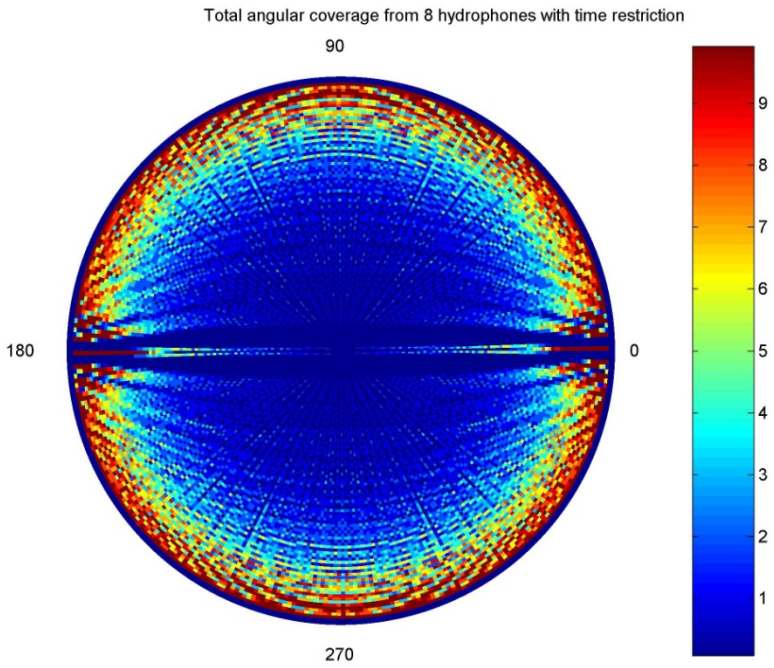

Figure 4.20 Angular shot density for initial configuration

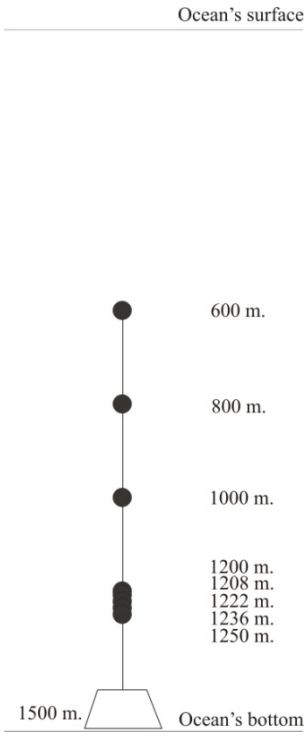

Figure 4.21 Configuration of available equipment

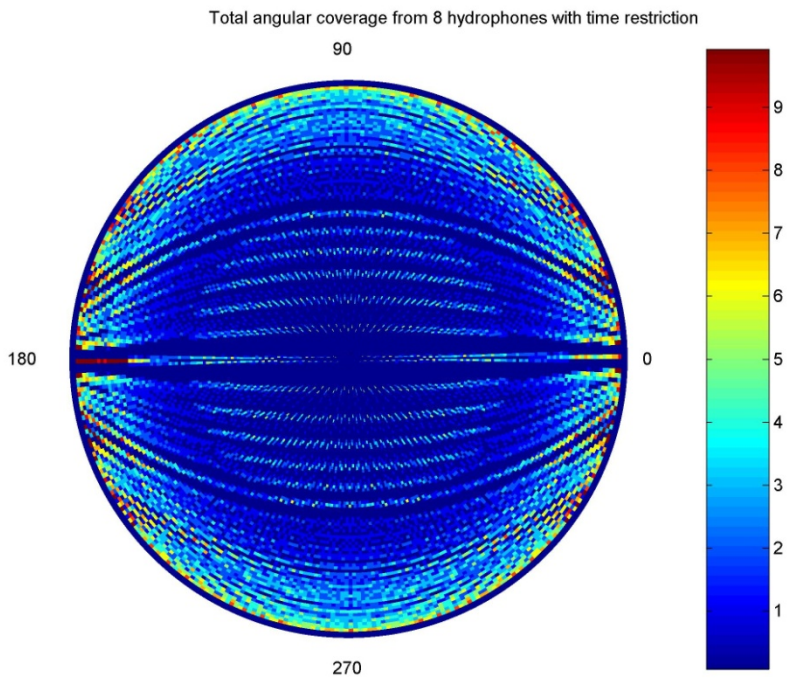

Figure 4.22 Angular shot density for available equipment

At that point LADC had two arrays with 200 m spacing between hydrophones, 4 arrays with 14 m spacing between hydrophones, and 4 arrays with 7 m spacing between hydrophones. Collocation of ambient and desensitized hydrophones gave flexibility in the measurement of the source array in the near field by spreading the hydrophone depths from 100 meters up to 1200 meters along the mooring's main line. Simulation results suggested hydrophones placed at 100m, 300m, 531m(including an extra 31 m for flotation), 731m, 920m, 934m, 948m, and 962m on one of the long moorings, and at 1150m, 1157m, 1171m, and 1163m, on a short deep water mooring. The long mooring used the two long arrays and two of the 14 m. spacing arrays. The deep mooring used the two 7 m. spacing arrays. The PSG supported the purchase of two additional 200 m. spacing arrays to be used with the two remaining 14 m. arrays to make an additional mooring for redundancy. The entire second mooring was deployed with a slight vertical shift by 50 meters, giving a total of 16 independent hydrophone depths on the long moorings. The short deep water mooring was used to fill in the close-to-vertical emission angles with enough data. In addition to the bottom moorings, eight hydrophones (giving 4 hydrophone depths) were deployed from the deck of the auxiliary ship used for equipment deployment and retrieval and environmental and positioning measurements.

Because of limited variations in shot line spacing and the limited variability of hydrophone depths on the mooring cables, the resulting emission angles received on the hydrophones are no longer equally spaced and the emission angle distribution is no longer uniform. In order to get an emission angle

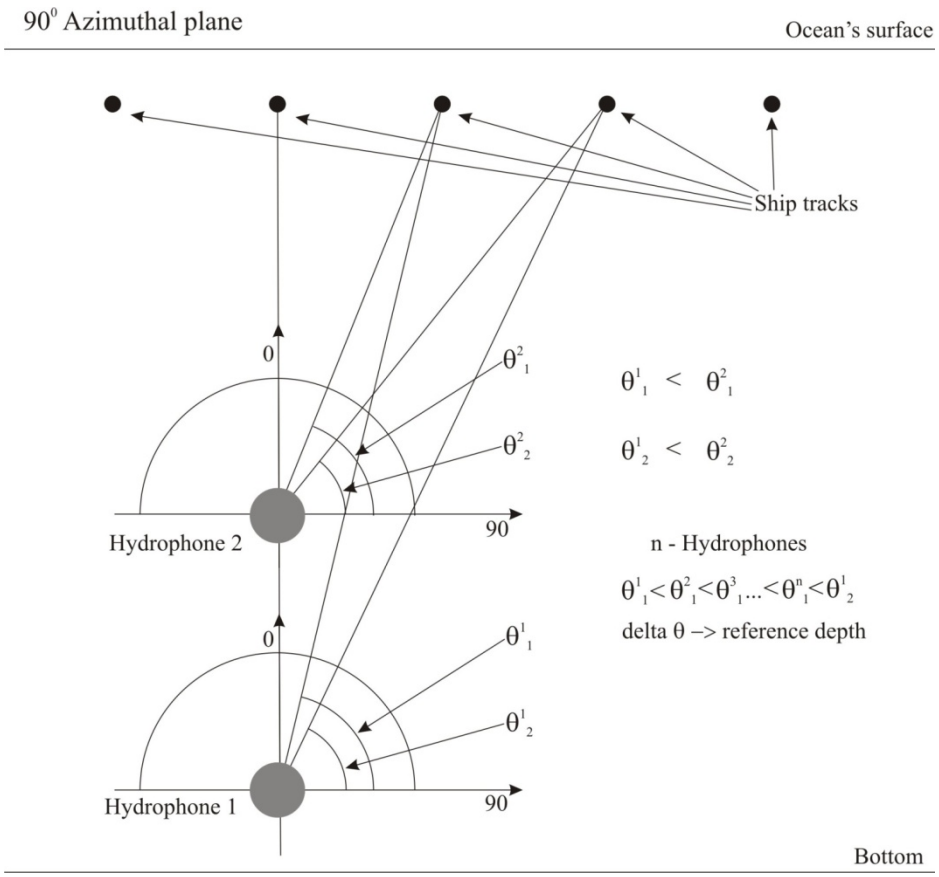

Figure 4.23 Uniform angular spacing for reference depth

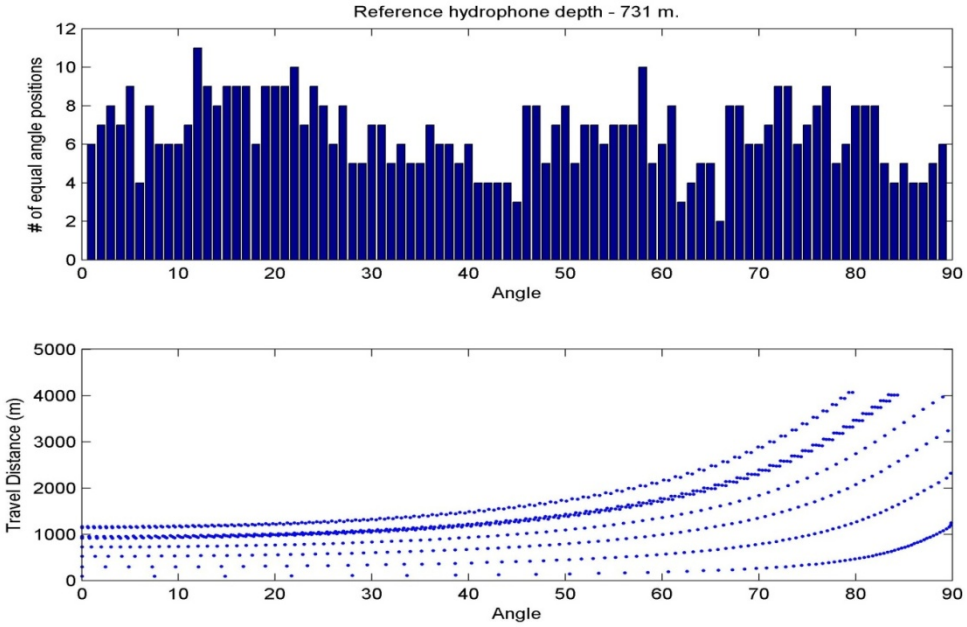

Figure 4.24 Optimal reference depth estimation

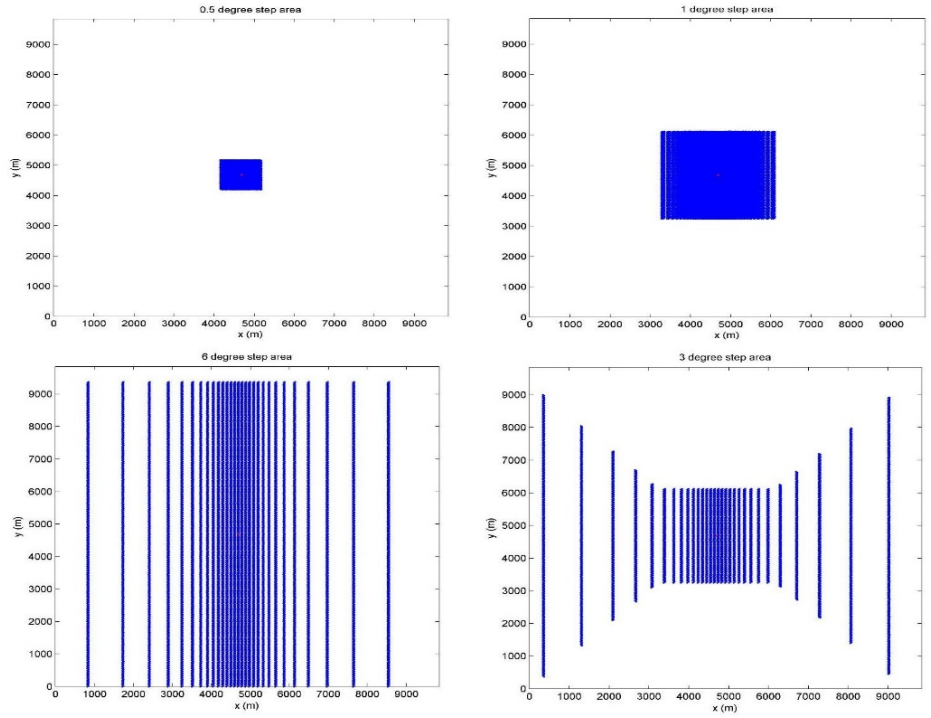

Figure 4.25 Proposed experimental separation of source ship tracks

distribution close to uniform, further numerical simulations were conducted. The main purpose of these simulations was to generate positions of ship tracks for a given uniform angular spacing for one reference depth (Figure 4.23) and to simulate received emission angles on hydrophone depths other than the chosen reference depth (Figure 4.24). By repeating the simulation for other reference depths we find the depth for which the overall emission angle distribution is close to uniform. After a series of simulations, a reference depth of 920 m was selected.

Due to overpopulation of the resulting angular shot density distribution for emission angles close to the horizontal, it was decided to save experimental time by dividing the experimental area into three different shot patches, a 0.5 degree patch, a 1 degree patch, and a 3 degree patch. The largest (9 km by 9 km) 3 degree patch covers emission angles from 0 to almost 90 degrees, with 3 degree spacing between emission angles received at the reference depth. The middle (2.5 km by 2.5 km.) 1 degree patch covers emission angles from 0 up to almost 60 degrees, with 1 degree spacing between emission angles received at the reference depth. The smallest patch (1 km by 1 km) covers emission angles from 0 up to 30 degrees with 0.5 degree spacing between emission angles received at the reference depth. Further analysis led to splitting the 3 degree area into two parts – 3 degree even-numbered lines and 3 degree odd-numbered lines. The 3 degree even line patch corresponds to a 6 degree patch. The 3 degree odd line patch has trapezoidal cutouts which result in reduced redundancy of overpopulated lines in the sail direction and

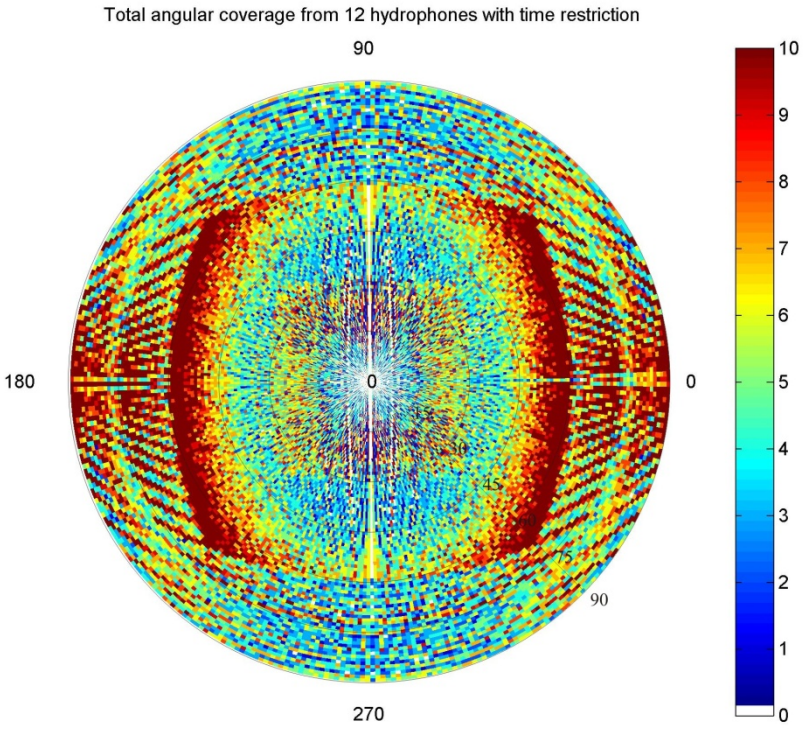

Figure 4.26 Angular shot density for proposed experimental source ship tracks

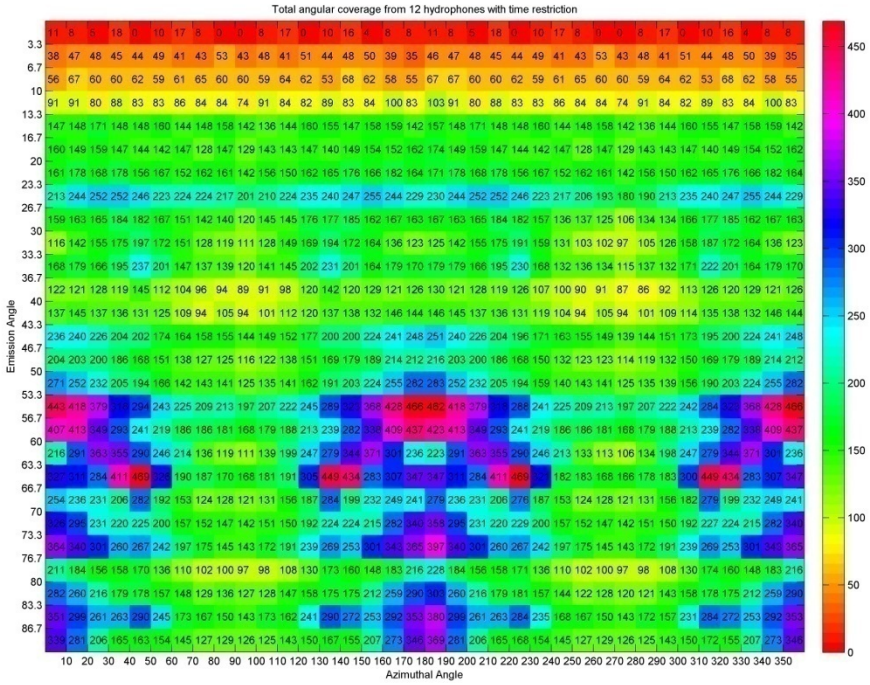

Figure 4.27 Angular space binning and shot density of shots from proposed ship tracks

thus save significant additional experiment time. All patches (including ship tracks for the 3 degree patch) are shown in Figure 4.25.

Angular shot density for 12 hydrophone depths (8 depths for one of the two long moorings and 4 depths for the deep water shot mooring) is shown in Figure 4.26. The color corresponds to the number of shots received for given emission and azimuthal angles calculated from simulation. The dark red color corresponds to angles with 10 or more received shots.

After long discussions with the PSG, due to uncertainty in array positioning systems and for purpose of statistical analysis, the existing solid angle domain was divided into angular bins with a 3.3 degree step for emission angles and a 10 degree step for azimuthal angles. The resulting distribution is shown in Figure 4.27. The color bar and numbers within bins correspond to estimated number of shots received on the hydrophones.

Conclusions and future research

The planned experiment was conducted in the northwestern part of the Gulf of Mexico September 2 – September 22, 2007. Three M/V were used during the experiment: the Fairfield Endeavor and the Veritas Vantage as a seismic array source ships, and the Cape Hatteras as an auxiliary ship for equipment deployment and retrieval and environmental and positioning measurements. For redundancy and for more near-vertical emission angle coverage, two additional moorings were deployed. An active tracking system and current profilers were used during the experiment to precisely log the three-dimensional positions of all individual hydrophone depths. Two additional hydrophone strings were ship deployed for shallow water measurements. Twenty four hydrophone depths with two collocated hydrophones at each depth (a sensitive hydrophone for ambient noise recording and a desensitized one for power shots) ranging from 10 meters (for ship-tethered hydrophones) to 1300 meters (for deep water buoys) were covered. The bottom depth for the experiment area varies from 1500 to 1600 meters. About 12 days of continuous acoustical broadband (up to 25 kHz) recordings and other auxiliary data measurements (sound speed profiles, bathymetry, etc.) were collected during the experiment. In addition, two long distance propagation lines (needed for propagation model validation) were collected. The total amount of data collected is about 3.6 terabyte.

All collected data were checked for errors and misreading. By using a simple propagation model based on ray tracing, primary shot arrivals from the seismic exploration array were extracted and at the present time are being analyzed. Acoustical equipment used in the experiment is being post calibrated. Results of post calibration and visual data checks will be published in the near future. After an uncertainty analysis of the positioning equipment, the angular domain is divided into angular bins, with 3.3 degree bin width for emission angles and 10 degree bin width for azimuthal angles. Collected data will be analyzed on a single line basis and within angular bins. The large amount of data measurements allows statistical analysis. In the case of missing coverage, data necessary for a three-dimensional characterization will be modeled using techniques described in Chapter 3. Results will be presented in three-dimensional visualizations.

References

ANSI/ASA ANSI S1.11-2004. American National Standard Specification for Octave-Band and Fractional-Octave-Band Analog and Digital Filters - SAME AS ASA 65 American National Standards of the Acoustical Society of America / 19-Feb-2004 / 29 pages.

Au, W. W. L., Nachtigall, P. E., and Pawloski, J. L. (1997). "Acoustic effects of the ATOC signal (75 Hz, 195 dB) on dolphins and whales," J. Acoust. Soc. Am. 101, 2973-2977.

Bayin S. S. (2006), Mathematical Methods in Science and Engineering, Wiley, Chapters 18 and 19.

Blackwell, S. B., Lawson, J. W., and Williams, J. T. (2004). "Tolerance by ringed seals (Phoca hispida) to impact pipe-driving and construction sounds at an oil production island," J. Acoust. Soc. Am. 115, 2346–2357.

Caldwell, J., and Dragoset, W. (2000). "A brief overview of seismic air-gun arrays," The Leading Edge 19, 898–902.

Collins, M. D. (1993). "A split-step Padé solution for the parabolic equation method," J. Acoust. Soc. Am. 93, 1736–1742.

DeRuiter, S.L., Tyack, P.L., Lin, Y-T., Newhall, A.E., Lynch, J.F., Miller, P.J.O. (2006). "Modeling acoustic propagation of air gun array pulses recorded on tagged sperm whales (Physeter macrocephalus)," J. Acoust. Soc. Am. 120, 4100-4114.

Fricke, J.R., Davis, J.M., Reed, D.H. (1985). "A standard quantitative calibration procedure for marine seismic sources," Geophysics 50 (10), 1525-1532.

Gordon, J., Gillespie, D., Potter, J., Frantzis, A., Simmonds, M. P., Swift, R., and Thompson, D. (2004). "A review of the effects of seismic surveys on marine mammals," Mar. Technol. Soc. J. 37, 16–34.

Hamilton, E. L. (1980). "Geoacoustic modeling of the sea floor," J. Acoust. Soc. Am. 68, 1313–1340.

Hatton, L. (2002). "Gundalf - a software package for predicting the acoustic signature of high pressure airguns in exploration seismology," in 'http://www.gundalf.com/' (last viewed on August 1, 2007).

Hatton, L. (2004). "Incorporating marine mammal hearing sensitivity into a high-grade air gun modelling package (extended abstract)," in PETEX 2004, November 2004.

Ioup, G.E., Ioup, J.W., Sidorovskaia, N.A., Walker, R.T., Kuczaj, S.A., Walker, C.D., Rayborn, G.H., Brack, B., Wright, A., Newcomb. J., and Fisher, R. (2005). "Analysis of Bottom-Moored Hydrophone Measurements of Gulf of Mexico Sperm Whale Phonations," in Proceedings of 23rd Annual Gulf of Mexico Information Transfer Meeting, January 2005, pp. 109-136.

Johnston , R.C., Reed, D.H., Desler, J.F. (1988). "Special Report of the SEG Technical Standards Committee SEG standards for specifying marine seismic energy sources," Geophysics 53 (4), 566-575.

Kinsler, L.E., Frey, A.R., Coppens, A.B., and Sanders, J.V., Fundamentals of acoustics, Wiley, New York (1982)

Labianca, F. M. (1972). "Normal modes, virtual modes, and alternative representations in the theory of surface-duct sound propagation," J. Acoust. Soc. Am. 53, 1137–1147.

Laws, R.M., Hatton, L., and Haartsen, M.W. (1990). "Computer modelling of clustered airguns," First Break, Vol. 8, no. 9, pp.331-338.

Levy, M. Parabolic Equation Methods for Electromagnetic Wave Propagation, London, UK: IEE, 2000.

MacGillivray, A. O. (2006). "An acoustic modelling study of seismic airgun noise in Queen Charlotte Basin," M.Sc. Thesis, University of Victoria.

Madsen, P. T. (2005). "Marine mammals and noise: Problems with root mean square sound pressure levels for transients," J. Acoust. Soc. Am. 117, 3952–3957.

Madsen, P. T., Johnson, M., Miller, P. J. O., Aguilar de Soto, N., Lynch, J., and Tyack, P.L. (2006). "Quantitative measures of air gun pulses recorded on sperm whales (Physeter macrocephalus)

using acoustic tags during controlled exposure experiments," J. Acoust. Soc. Am. 120, 2366–2379.

Monjo, C.L., and DeFerrari, H.A. (1994). "Analysis of pulse propagation in a bottom-limited sound channel with a surface duct," J. Acoust. Soc. Am. 95, 3129-3148.

Newcomb, J., Fisher, R., Turgut, A., Field, R., Ioup, G.E., Ioup, J.W., Rayborn, G., Kuczaj, S., Caruthers, J., Goodman, R., and Sidorovskaia, N. (2002a). "Modeling and Measuring the Acoustic Environment of the Gulf of Mexico," in Proceedings of the 21-st Annual Gulf of Mexico Information Transfer Meeting, January 2002, 509-521.

Newcomb, J., Fisher, R., Field, R., Rayborn, G., Kuczaj, S., Ioup, G.E., Ioup, J.W., Turgut, A. (2002b). "Measurements of Ambient Noise and Sperm Whale Vocalizations in the Northern Gulf of Mexico Using Near Bottom Hydrophones," MARINE FRONTIERS MTS/IEEE Proceedings of OCEANS'02, 1365-1371.

Newcomb, J., Sanders, W., Stephens, J.M., Walker, C., Brack, B., Rayborn, G.H., Sidorovskaia, N.A., Tashmukhambetov, A.M., Ioup, G.E., Ioup, J.W., and Chapin, S.R. (2005). "Calibration and Analysis of Seismic Air gun Data from an EARS Buoy," in Proceedings of 23rd Annual Gulf of Mexico Information Transfer Meeting, January 2005, 83-100.

Porter, M. B. (1995). The KRAKEN Normal Mode Program (SACLANT Undersea Research Center, La Spezia, Italy).

Richardson, W.J., Greene, Jr., C.R. , Malme, C.I., and Thomson, D.H. (1995). Marine mammals and noise (Academic Press, San Diego, CA).

Sidorovskaia, N.A. (2004). "Systematic studies of pulse propagation in ducted oceanic waveguides in normal mode representation," The European Physical Journal, Applied Physics 25 (2), 113-131.

Sidorovskaia, N.A., and Werby, M.F. (1995). "Broad-band pulse signals and the characterization of shallow water ocean properties," in Proceedings of the SPIE Conference, April 1995, 97-108.

Sidorovskaia, N.A., Ioup, G.E., Ioup, J.W., Tashmukhambetov, A.M., Newcomb, J.J., Stephens, J. M., and Rayborn, G. H. (2006). "Modeling tools for 3-d air gun source characterization studies," in Proceedings of the eighth European Conference on Underwater Acoustics, June 2006, edited by S.M. Jesus and O.C. Rodriguez, 95-100.

Smith, K.B., and Tappert, F.D. (1993). "UMPE: The University of Miami Parabolic Equation Model, Version 1.3," MPL Technical Memorandum 432.

Southall, B. L., Schusterman, R. J., and Kastak, D. (2000). "Masking in three pinnipeds: underwater, low-frequency critical ratios," J. Acoust. Soc. Am. 103, 1322–1326.

Southall, B. L., Schusterman, R. J., and Kastak, D. (2003). "Acoustic communication ranges for northern elephant seals (Mirounga angustirostris)," Aquatic Mammals 29.2, 202–213.

Tashmukhambetov, A.M., Sidorovskaia, N. A., Ioup, G.E., Ioup, J.W., Newcomb, J., Walker, C., Brack, B., Rayborn, G.H. (2006). "3-D airgun source characterization and propagation modeling," in SEG Technical Program Expanded Abstracts 25, 26-30, doi:10.1190/1.2370084.

Tashmukhambetov, A.M., Ioup, G.E., Ioup, J.W., Sidorovskaia, N.A., and Newcomb, J.J (2008) "Three-dimensional seismic array characterization study: Experiment and modeling", Jour. Acoust. Soc. Am. 123, 4094-4108.

Tashmukhambetov, A.M., Ioup, G.E., Ioup, J.W., Sidorovskaia, N. A., Newcomb, J., Stephens, J.M., and Rayborn, G.H. "Source Characterization Study 2007: The three-dimensional primary field of a seismic airgun array", paper presented at the Acoustical Society of America, Portland, OR, 18-22 May 2009, and abstracted in Jour. Acoust. Soc. Am. 125, 2539

Tashmukhambetov, A.M., Sidorovskaia, N. A., Ioup, G.E., Ioup, J.W., "Modeling the three-dimensional field of a seismic airgun array and comparison to 2003 measured data", presented at the Acoustical Society of America, Miami, FL, 10-14 Nov 2008, and abstracted in Jour. Acoust. Soc. Am. 124, 2599

Tashmukhambetov, A.M., Ioup, G.E., Ioup, J.W., Sidorovskaia, N. A., Newcomb, J., Stephens, J.M., and Rayborn, G.H. “The source characterization study 2007: A detailed three dimensional acoustic field measurement of a seismic airgun array”, presented at the Acoustical Society of America, Miami, FL, 10-14 Nov 2008, and abstracted in Jour. Acoust. Soc. Am. 124, 2599

Tolstoy, M., Diebold, J. B., Webb, S. C., Bohnenstiehl, D. R., Chapp, E., Holmes, R. C., and Rawson, M. (2004). “Broadband calibration of R/V Ewing seismic sources,” Geophys. Res. Lett. 31, L14310, doi:10.1029/2004GL020234.

Turgut, A., McCord, M., Newcomb, J., and Fisher, R. (2002). “Chirp sonar sediment characterization at the northern Gulf of Mexico Littoral Acoustic Demonstration Center experimental site,” Oceans '02 MTS/IEEE 4, 2248–2252.

Ziolkowski, A. (1970). “A method for calculating the output pressure waveform from an air gun,” Geophys. J. R. Astron. Soc. 21, 137–161.

Ziolkowski, A., Parkes, G., Hatton, L., and Haugland, T. (1982). “The signature of an air gun array: Computation from near-field measurements including interactions,” Geophysics 47, 1413–1421.

Vita

Arslan M. Tashmukhambetov was born in Almaty, Kazakhstan, on June 24, 1980. He attended Gymnasium # 111 and graduated in May, 1997. Then he attended the Kazakh State University, earning a B.S. degree in Physics in May 2003. After graduation from Kazakh State University he attended the University of Louisiana at Lafayette, graduating in May 2005 with an M.S. degree in Applied Physics. In June 2005 he entered the Engineering and Applied Science Ph.D. program at the University of New Orleans. Since May 2003 he has been continuously working as a graduate research assistant with participants of the LADC (Littoral Acoustic Demonstration Center) group. He will earn his Ph.D. in Engineering and Applied Sciences in August, 2009.